University of California

Ernest O. Lawrence Radiation Laboratory

NOISE CONSIDERATIONS IN NUCLEAR PULSE AMPLIFIERS

Berkeley, California

DISCLAIMER

This report was prepared as an account of work sponsored by an agency of the United States Government. Neither the United States Government nor any agency Thereof, nor any of their employees, makes any warranty, express or implied, or assumes any legal liability or responsibility for the accuracy, completeness, or usefulness of any information, apparatus, product, or process disclosed, or represents that its use would not infringe privately owned rights. Reference herein to any specific commercial product, process, or service by trade name, trademark, manufacturer, or otherwise does not necessarily constitute or imply its endorsement, recommendation, or favoring by the United States Government or any agency thereof. The views and opinions of authors expressed herein do not necessarily state or reflect those of the United States Government or any agency thereof.

DISCLAIMER

Portions of this document may be illegible in electronic image products. Images are produced from the best available original document.

UNIVERSITY OF CALIFORNIA

Lawrence Radiation Laboratory
Berkeley, California

Contract No. W-7405-eng-48

NOISE CONSIDERATIONS IN NUCLEAR PULSE AMPLIFIERS

Donald A. Landis

(M.S. Thesis)

December 20, 1961

NOISE CONSIDERATIONS IN NUCLEAR PULSE AMPLIFIERS

Table of Contents

NOISE CONSIDERATION IN NUCLEAR PULSE AMPLIFIERS

Donald A. Landis

Lawrence Radiation Laboratory
University of California
Berkeley, California

December 20, 1961

ABSTRACT

This paper considers the effects of certain pulse-shaping networks on the signal-to-noise ratio of a nuclear pulse amplifier. The shaping networks discussed are: (1) equal RC-integrating and RC-differentiating time constant, (2) single-delay-line clipper and RC integrator, and (3) double-delay-line clipper and RC integrator.

The effects of these networks on the signal, when high count rates and overload pulses are present, are also considered. Equations and curves are developed for the energy resolution (signal-to-noise ratio) and resolving time (related to the ability to operate at high counting rates) of the networks.

Experimental results are shown for the energy resolution of the types of pulse-shaping networks considered.

I. INTRODUCTION

This paper reviews the sources of noise in nuclear pulse amplifiers, and considers the effects of pulse-shaping networks contained in the amplifier in optimizing the performance of counting systems. In some cases, the pulse-shaping circuits in the amplifier are selected to give a maximum signal-to-noise ratio. In others, the shaping circuits are selected to compromise between the signal-to-noise ratio and the ability of the amplifier to handle high input-signal rates. Both aspects are considered in this paper.

The amplifier is one component in a system used to determine the characteristics of nuclear particles, such as the energy of alpha or beta particles and gamma rays. Figure 1 (a) is a block diagram of a typical system used to measure the energy of alpha particles. The detector converts the absorbed energy of the alpha particles into electrical charge pulses. The charge is then applied to a linear pulse amplifier that shapes and amplifies the signal. The signal from the amplifier is applied to a pulse-height analyzer that determines the amplitude distribution of the pulses. Means are provided to display the distribution for visual observation. Test pulses applied to the input of the amplifier are used to calibrate and check the performance of the system. A typical amplitude distribution is shown in Fig. 1 (b). The horizontal axis represents the pulse amplitude scale which, in most systems, is linearly related to the energy of the alpha particles; the vertical axis represents the number of counts or pulses received in the counting time in a small predetermined amplitude range. Peaks corresponding to alpha-particle pulses and the test pulses can be seen in the figure. The test peak is generally narrower than the alpha peak because the test pulses are modulated only by electrical noise at the input of the amplifier. The additional spread in the alpha peak is caused by defects in the detector. The capability of the system to resolve two alpha particles of nearly equal energy is directly related to the amount of spread of the energy peak, and is usually expressed as the full width of the peak at half of its

(a)

Alpha source
5 Mev

(b)
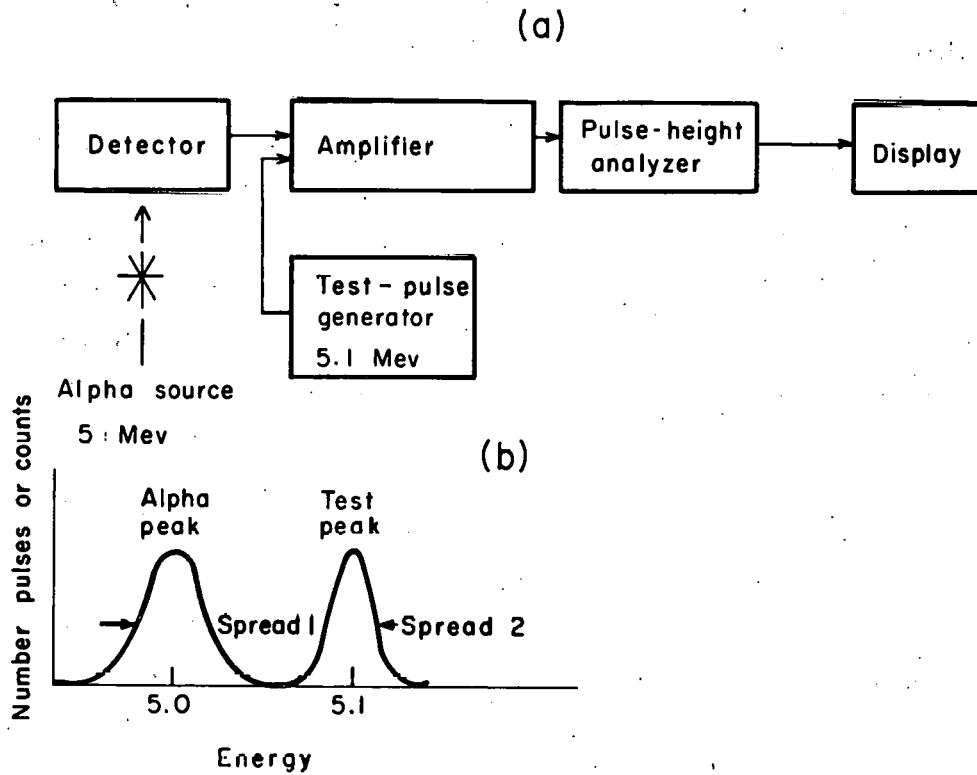
Fig. 1. (a) Block diagram of a system for measuring alpha
particles. (b) Distribution of pulse amplitudes from the
pulse-height analyzer.

maximum amplitude, here abbreviated as FWHM. Resolution depends on the signal-to-noise ratio of the amplifier system. In this paper, the signal is defined as the peak amplitude of the pulse at the output of the amplifier, and the noise is defined as the RMS (root-mean-square) noise voltage at the output. The noise is assumed to cause pulses having the same amplitude at the input of the amplifier to also have a gaussian amplitude distribution at its output. Figure 2 shows the relation between the RMS and FWHM spreads in amplitude of the pulses from the amplifier. The FWHM spread is about 2.35 times the RMS spread (σ), where σ is a standard deviation of the Gaussian peak.[1]

Improving the energy resolution by a small amount may be important when energies are being measured for alpha groups that have peaks very close together in energy. This is illustrated in Fig. 3 by the three curves of alpha peaks from Pu^{238}, which are 44 kev apart with FWHM energy resolutions of (a) 20 kev, (b) 30 kev, and (c) 40 kev. The 5.496-Mev peak occurs at a rate that is about 2.5 times that of the 5.452-Mev peak. The 40-kev resolution curve appears to have only one peak, but both peaks are apparent in the 30- and 20-kev curves. This shows that the improvement in energy resolution from 40 to 30 kev, i ... though small, was needed to reveal both peaks.

In experiments operated at high count rates, it is as important to consider resolving time as to consider FWHM energy resolution due to noise. Here the resolving time is defined as the time for the response of an impulse of charge applied to the amplifier input to decay down to some percentage of its maximum amplitude. If a pulse from the amplifier falls on the tail of a preceding pulse, the second pulse is displaced in amplitude. This displacement may either cause an asymmetrical spread in the peak of the energy-resolution curve, or cause false peaks to appear.

The types of pulse-shaping circuits considered in this paper are: (a) RC shaping, which consists of an RC integrator and an RC differentiator with equal time constants in cascade (see Fig. 22); (b) single delay-line shaping, which consists of a delay-line clipper together with
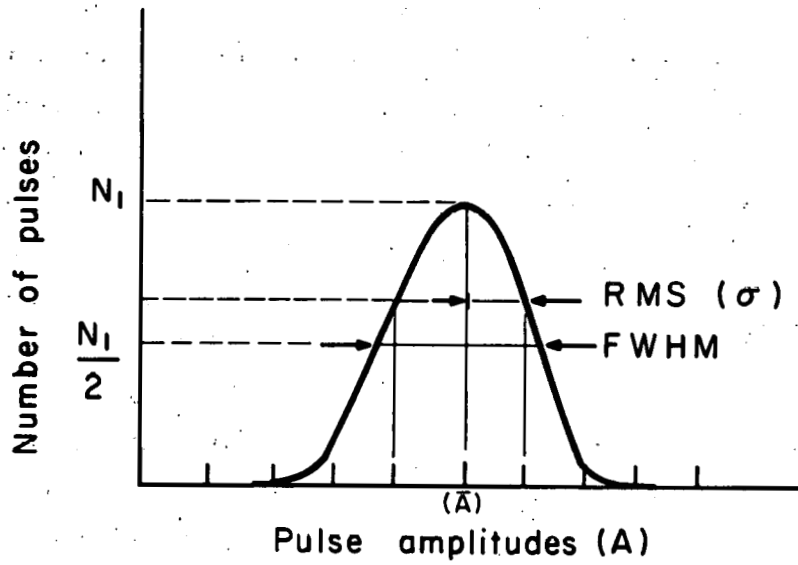
MU-25416

Fig. 2.   Plot of FWHM = 2.355 σ for a Gaussian distribution,
where σ is the standard deviation.
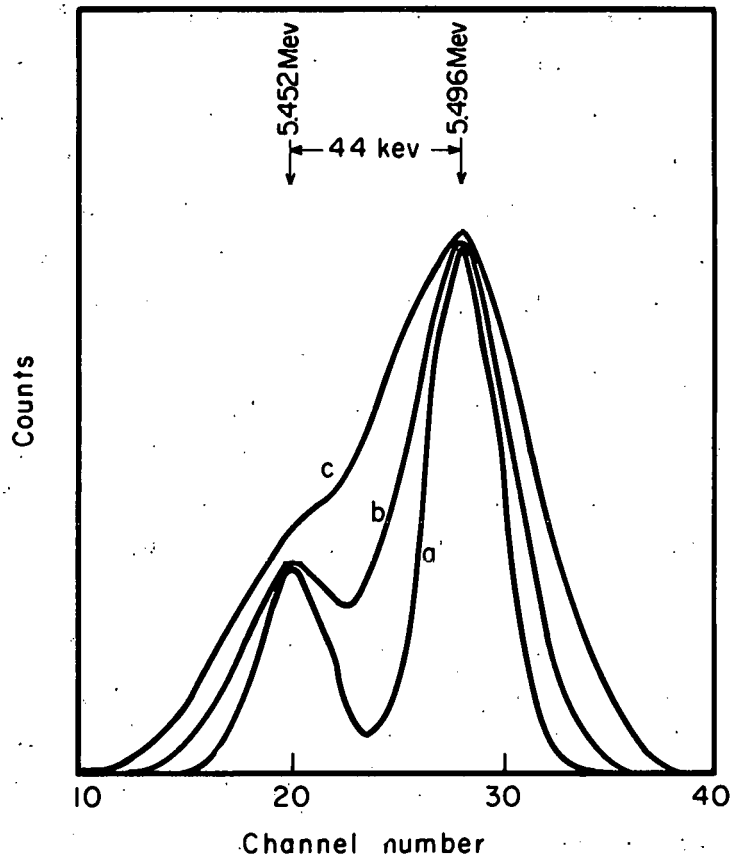
Fig. 3. Energy spectrum of Pu^{238} (two alpha peaks) for FWHM energy resolutions of (a) 20 kev, (b) 30 kev, and (c) 40 kev. The energy of each channel is approx 11 kev.

an RC integrator (see Fig. 24); and (c) double-delay-line shaping, which consists of two delay-line clippers and an RC integrator, all in cascade (see Fig. 27).

The RC shaping is the simplest type and is generally used because it is the easiest to optimize with respect to energy resolution for a given system. It has been shown that for RC shaping there is an optimum time constant for a given system, giving the best signal-to-noise ratio or energy resolution.[2] In some situations, however, a slight improvement in energy resolution can be obtained by using single-delay-line shaping. In other situations, single-delay-line shaping improves the resolving time. Neither RC nor single-delay-line shaping can be used at very high count rates. Double-delay-line shaping has poorer energy resolution because of noise than the first two methods, but is much more desirable at high counting rates and when high-energy extraneous pulses cause the amplifier to momentarily overload. This is true because double-delay-line shaped pulses are symmetrical about the base line and tend to reduce base-line shift with changes in count rates and overloads.

Figure 4 shows several pulse shapes from the amplifier and their corresponding amplitude spectrum qualitatively, obtained with a pulse-height analyzer when the system is operated at high count rates. Figure 4 (a) shows an RC-shaped pulse followed by a second RC differentiator with a long time constant. The second differentiator causes the pulse to have an undershoot with a long decay. The pulse-amplitude spectrum shows a spread of the peak on its lower-amplitude side when the tail of one pulse has not decayed back to the base line before another pulse appears. The dotted lines on the amplitude spectrum curves are the amplitude spectrums when the system is operated at low count rates. Figure 4 (b) shows the effect of an RC-shaped pulse followed by two more differentiating circuits in cascade. Note that there is an undershoot and an overshoot on the tail of the pulse from the amplifier. This gives a corresponding spread in the amplitude spectrum on both sides
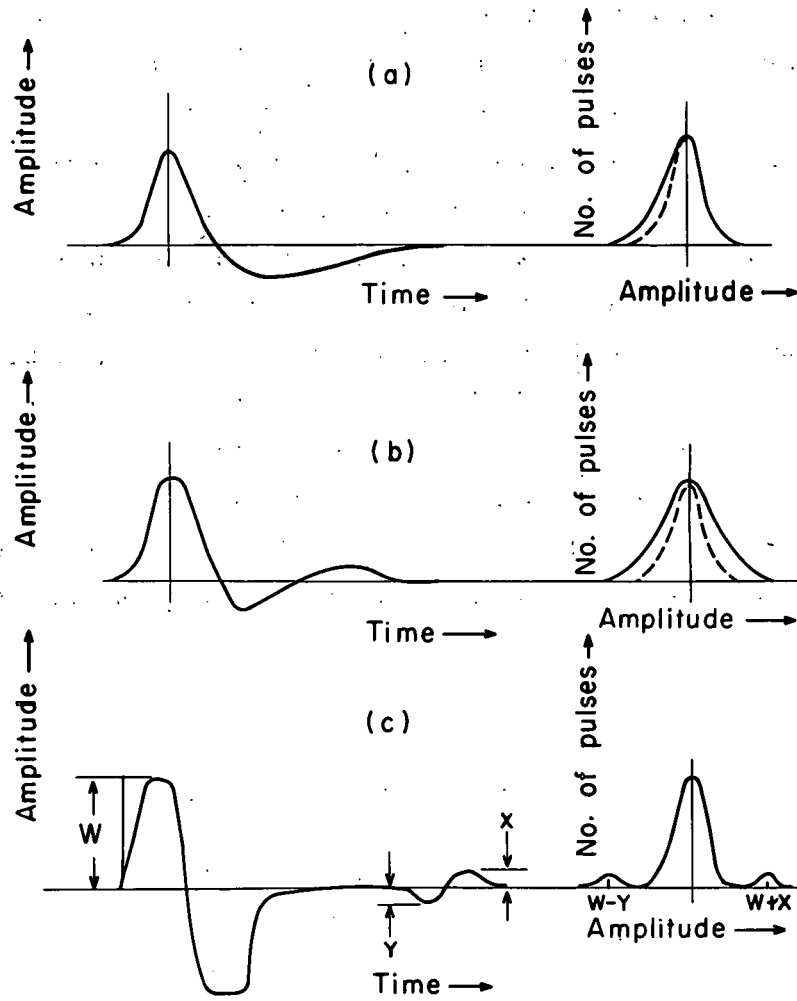
Fig. 4. Shaped pulses from the amplifier, with their amplitude
spectrum at high count rates: (a) RC shaped pulse plus
another differentiator; (b) RC shaped pulse plus two
differentiators; and (c) double-delay-line shaped pulse
with a small reflection.

of the peak, when the amplifier is operated at high count rates. All
RC-shaped amplifiers exhibit some over- and undershoot on the tail of
the pulses from the amplifier because of the normal RC coupling between
stages, and therefore cause spreading of the amplitude spectrum at
high count rates. For this reason, RC shaping is usually not used at
high count rates. Figure 4 (c) shows a double-delay-line shaped pulse
that was followed by a small reflected pulse because it had a long, im-
properly terminated transmission line on the output of the amplifier.
False peaks are produced in the amplitude spectrum when the amplifier
is operated at high count rates, because a few pulses fall on top of the
reflections from preceding pulses. This can be very undesirable when
measurements of weak alpha groups are being made, because it is hard
to differentiate the false peaks from the real peaks. For this reason
the time it takes the pulse to decay from 10% to about 0.1% of its peak
amplitude is more important than the total resolving time.

II. NUCLEAR PARTICLE DETECTORS

The type of particle detector used to analyze the energy resolution and resolving time of the amplifier must be considered, because the detector determines the characteristics of the signal applied to the amplifier. The types of detector generally used to detect alpha and beta particles are scintillation counters, ionization chambers, and semiconductor detectors. Scintillation counters are not usually used when good energy resolution from alpha particles is desired. Ionization chambers have been used for many years, and FWHM energy distributions of 27 kev have been obtained with them.[3] The semiconductor detector on the other hand, has only been in use for the last few years. It promises to give much better energy resolution than ionization chambers do, because it produces ten times as much signal for a particular absorbed particle energy. In a gas ionization chamber, 27 to 35 electron volts are required to create an ion-electron pair, depending on the gas used. In a semiconductor detector the corresponding energy is approx 3.4 ev for each hole-electron pair. In addition, these detectors are quite small in size, and therefore have very short collection times. The ionization chamber and the semiconductor detector can be considered to be capacitances that receive some charge in a collection time Δt, owing to the absorption of energy of the nuclear particle.

The semiconductor detector is a silicon p-n junction diode that is back-biased with a voltage that may range from several volts to several hundred volts. A current noise source must be included across the capacitance in the equivalent circuit for the semiconductor detector because there is leakage current in the back-biased junction of the detector. Detectors have been produced that reduce surfaceleakage so that the leakage current is mainly bulk leakage.[4] The capacitance of the detector is usually assumed to be that of a parallel-plate capacitor with its plates separated by a distance equal to the depletion layer width.[5] Figure 5 shows a simple equivalent circuit of the semiconductor detector. The charge produced across the capacitor is about 1.6×10^{-19} coulombs for

(a)

(b)
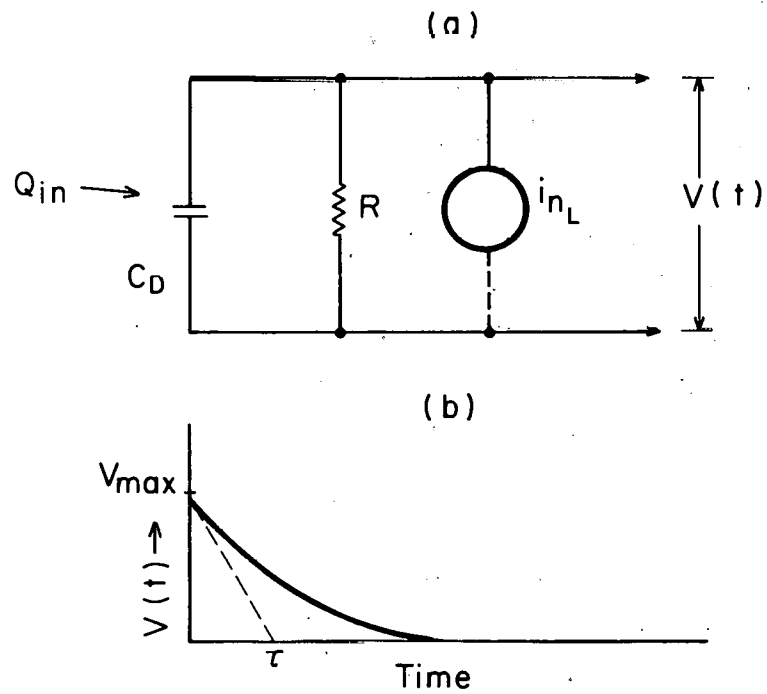
MU-25419

Fig. 5. (a) Equivalent circuit of the semiconductor detector, where R is the shunt resistance of the detector bias and amplifier input circuits. (b) Voltage produced for an impulse of charge applied to the detector, where $V_{max} = Q_{in}/C_D$, and $\tau = RC_D$.

every 3.5 ev of energy absorbed by the detector. More precise equivalent circuits for the detector have been suggested,[6] but they will not be used in this analysis. The signal from the detector is usually a very fast rising pulse with a long decaying tail produced by discharge of the capacitor through the detector biasing and amplifier input circuits.

III. PREAMPLIFIER CONSIDERATION

The first stage in the amplifier is actually a special low-noise preamplifier, placed as close to the detector as possible. A cable is connected from the output of the preamplifier to the rest of the amplifier. Several types of preamplifier may be used. One is the high-input-impedance type and another is the integrator or charge-sensitive type. Figures 6 and 7 shows simple circuits of these two types of preamplifiers. The output voltage V_0 of the high-input-impedance preamplifier is a function of the detector capacitance, and therefore is a function of the detector bias. The detector bias may change over a period of time and cause the output voltage to change. The system would need to be recalibrated with a change in bias voltage if the high-input-impedance preamplifier is used.

The integrator preamplifier has a transfer function that is almost independent of the detector capacitance because of the very large equivalent capacitance across the input of the preamplifier. (Transfer function (K) is the ratio of voltage-out to charge-in, or $K = V_0/Q_{in}$.) The optimum energy resolution obtained from the integrator preamplifier is poorer than the resolution for the high-input-impedance preamplifier, because of the added capacitance across the input from feedback capacitor C_f. The added advantage of being able to change the detector bias voltage without changing the gain of the preamplifier usually more than compensates for the poorer resolution of the integrator preamplifier. There are many texts that analyze preamplifiers, so they are not considered in detail in this paper.[7]
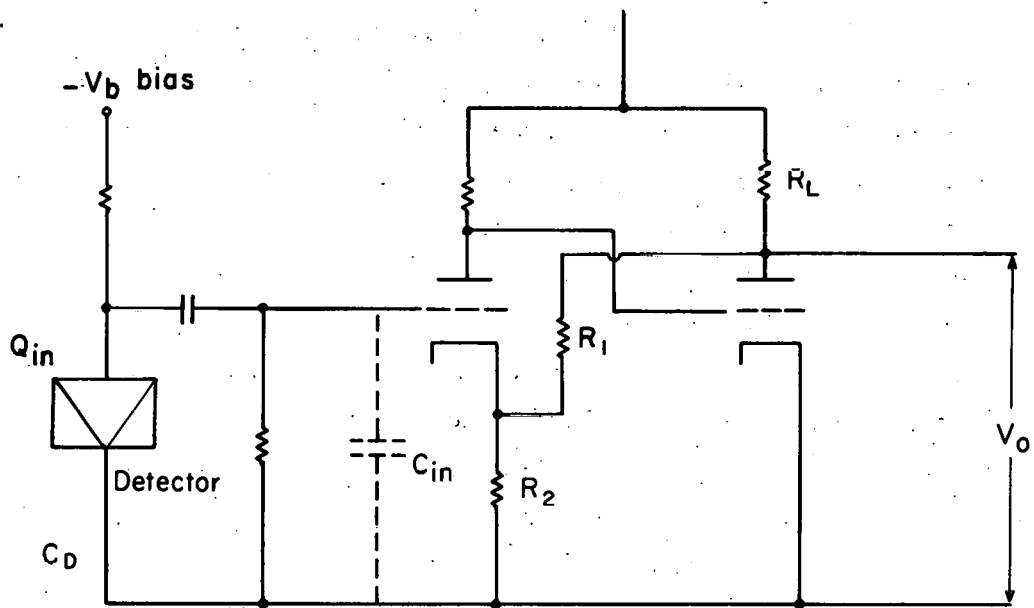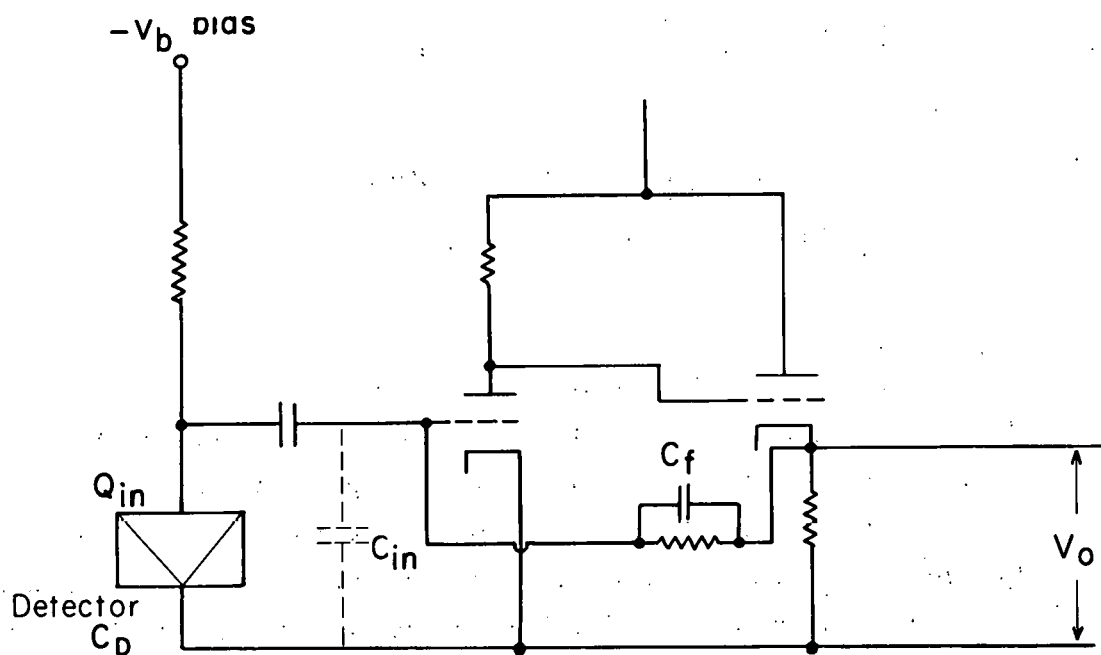
MU-25420

Fig. 6. High-input-impedance preamplifier, with

$$V_0 \approx \frac{\dfrac{G\,Q_{in}}{1 + G\beta}}{C_D + C_{in}} \approx \frac{Q_{in}}{\beta(C_D + C_{in})} \quad ,$$

where G is the open-loop gain, and $\beta \approx R_2/R_1$ for $R_L \gg R_1 + R_2$.

MU-25421

Fig. 7. Integrator amplifier, with

$$V_0 \approx \frac{-Q_{in} \, G}{C_D + C_{in} + GC_f} \approx \frac{-Q_{in}}{C_f} \,,$$

for : $C_f G \gg C_D + C_{in}$.

IV. DETECTOR AND AMPLIFIER NOISE SOURCES.

The main sources of noise in the particle energy measuring system are the detector and the first stage of the preamplifier. This is true if the power gain in the first stage is sufficient to make the noise of later stages insignificant, as shown in Eq. (1).[8]

$$F_t = 1 + F_1 - 1 + \frac{F_2 - 1}{G_1} + \frac{F_3 - 1}{G_1 G_2} , \qquad (1)$$

where

F_t = noise figure for total system,

F_a = noise figure for stage a,

a = 1, 2, 3, etc.,

and

G_a = available power gain from stage a.

The noise figure of the total system is approximately equal to the noise figure of the first stage, if the available gain of the first stage is large. The sources of noise in the detector and the first stage are: (a) shot noise in the tube, (b) grid current in the tube, (c) leakage current in the detector, (d) Johnson noise from the real part of the source impedance (bias resistor, etc.), and (e) flicker noise in the tube.
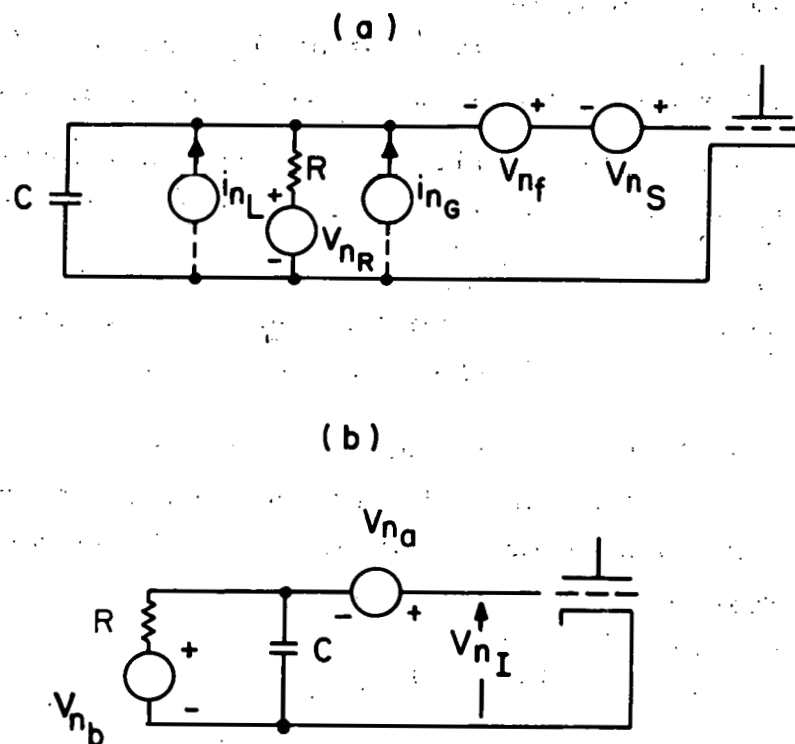
A. Noise Sources Referred to Preamplifier Input

The noise sources referred to the input of the preamplifier are shown in Fig. 8 (a), and these are defined as follows:

$\langle V_{n_s}^2 \rangle_{av}$ = Mean square shot noise, referred to the input of the tube = $4 kT R_{eq} df$, (2)

$\langle i_{n_G}^2 \rangle_{av}$ = Mean square grid current noise = $2q(|I_{g_e}| + |I_{g_c}|) df$, (3)

$\langle i_{n_L}^2 \rangle_{av}$ = Mean square leakage current noise = $2q(I_L) df$, (4)

$\langle V_{n_R}^2 \rangle_{av}$ = Mean square source resistance noise = $4kTR df$, (5)

(a)

(b)

MU-25422

Fig. 8 (a) The noise sources referred to the input of the
preamplifier. (b) The noise sources divided into
two groups – one affected by the RC circuit at the
preamplifier input, and one not.

and

$$\left\langle V_{n_f}^2 \right\rangle_{av} = \text{Mean square flicker noise, referred to the input}$$
$$= \frac{A}{f} df , \tag{6}$$

where

(a) Constant A has been determined experimentally[9] to be approximately 10^{-13},

(b) The equivalent noise resistance R_{eq} is about $2.5/g_m$,

(c) I_{g_c} is the electronic current collected by the grid (usually neglected for grid biases more negative than one volt),

(d) I_{g_e} is photo-electric electrons emitted by the grid, and can be approximated by Eq. 7,

(e) kT is Boltzmann's constant times the absolute temperature and is about 4×10^{-21} volt-coulombs at 25°C

and

(f) I_L is the bulk leakage current of the detector.

The grid current that is produced when soft x rays generated at the plate cause photoelectric electrons to be emitted by the grid can be approximated[10] by Eq. (7).

We then have:

$$I_{g_e} = (V_{gp})^{3/2} I_k \times 10^{-10} \text{ amp} , \tag{7}$$

where

V_{gp} = grid-to-plate voltage in volts,

I_k = cathode current in amperes.

It has been suggested that the grid current for most small tubes should be with-in a factor of 2 of Eq. (7), provided that[10]

(a) The grid bias be negative enough to cause the electronic component collected by the grid to be negligible,

(b) The tube be triode-connected,

(c) The control grid does not emit electrons thermionically,

(d) The tube be not operated at greater than 75% of its maximum plate dissipation so that outgassing is not significant,

and

(e) The tube be shielded from external light.

The different sources of the grid current are uncorrelated, so when there is more than one component of the grid current, the mean-squared noise from each component must be added together to get the total grid current noise.

B. Noise Sources Divided into Two Groups

The noise sources are divided into two groups–one that is affected by the RC circuit at the input of the preamplifier (detector and input capacitance and source resistance), and one that is not. These two sources are shown in Fig. 8(b), and may be formulated as:

$$\left\langle V_{n_a}^2 \right\rangle_{av} = \left\langle V_{n_s}^2 \right\rangle + \left\langle V_{n_f}^2 \right\rangle_{av} \tag{8}$$

and

$$\left\langle V_{n_b}^2 \right\rangle_{av} = \left\langle V_{n_R}^2 \right\rangle_{av} + R^2 \left\{ \left\langle i_{n_L}^2 \right\rangle_{av} + \left\langle i_{n_G}^2 \right\rangle_{av} \right\} \tag{9}$$

The total mean-squared noise applied to the grid is $\left\langle v_{n_I}^2 \right\rangle_{av}$ so that

$$\left\langle V_{n_I}^2 \right\rangle_{av} = \left\langle V_{n_a}^2 \right\rangle_{av} + \frac{\left\langle V_{n_b}^2 \right\rangle_{av}}{1 + \omega^2 R^2 C^2} , \tag{10}$$

where

$$C = C_{in} + C_D,$$

C_D = detector capacitance,

C_{in} = tube input and wiring capacitance,

ω = angular frequency,

R = total shunt resistance from grid to ground.

For the frequency range of interest, $\omega^2 C^2 R^2$ is made much greater than one; therefore:

$$\left\langle V_{n_I}^2 \right\rangle_{av} \cong \left\langle V_{n_a}^2 \right\rangle_{av} + \frac{\left\langle V_{n_b}^2 \right\rangle_{av}}{\omega^2 C^2 R^2} , \tag{11}$$

V. EFFECT OF THE FREQUENCY DEPENDENCE OF THE SHAPING CIRCUITS ON SIGNAL AND NOISE AT THE OUTPUT OF THE AMPLIFIERS

It is assumed in this paper that the shaping circuits determine the band-width of the amplifier, and consequently determine the noise band-width and shape of the output pulse. Figure 9 is a block diagram relating the noise source and frequency dependence of the amplifier, where $G(\omega)$ is the amplifier gain as a function of frequency (determined by shaping circuits).

The mean-square-noise voltage $\left\langle V_{n_0}^2 \right\rangle_{av}$ at the amplifier output can be found by integrating the product of the mean-squared-noise voltage at the amplifier input and the squared absolute value of the gain, which is a function of frequency, over the frequency range from zero to infinity. This output-noise voltage equation is

$$\left\langle V_{n_0}^2 \right\rangle_{av} = \frac{1}{2\pi} \int_0^\infty \frac{\left\langle V_{n_I}^2 \right\rangle_{av}}{df} \left| G(\omega) \right|^2 d\omega, \quad 2\pi\, df = d\omega \tag{12}$$

The input noise $\left\langle V_{n_I}^2 \right\rangle_{av}$ is obtained by combining Eqs. (2) through (6), (8), (9), and (11), and then has the form

$$\left\langle V_{n_I}^2 \right\rangle_{av} = \left[\frac{10\,kT}{g_m} + \frac{2\pi A}{\omega} + \frac{4\,kT}{R^2 C^2 \omega^2} + \frac{2q(I_G + I_L)}{C^2 \omega^2} \right] df. \tag{13}$$

The signal from the amplifier is the peak amplitude of the output pulse. The peak amplitude can be found if the input signal is assumed to be an impulse of charge applied to the input and detector capacitance C. This impulse of charge produces a step of voltage at the input equal to $V_{in} = Q_{in}/C$. The response of the amplifier to a unit step of voltage at the input is $H(t)$ as determined by the shaping circuits. The instant t_1 that the response is at a maximum can be found by setting the derivative of the response with respect to time equal to zero, and

$$\left\langle V_{n_I}^2 \right\rangle_{av} \qquad G(\omega) \qquad \left\langle V_{n_o}^2 \right\rangle_{av}$$
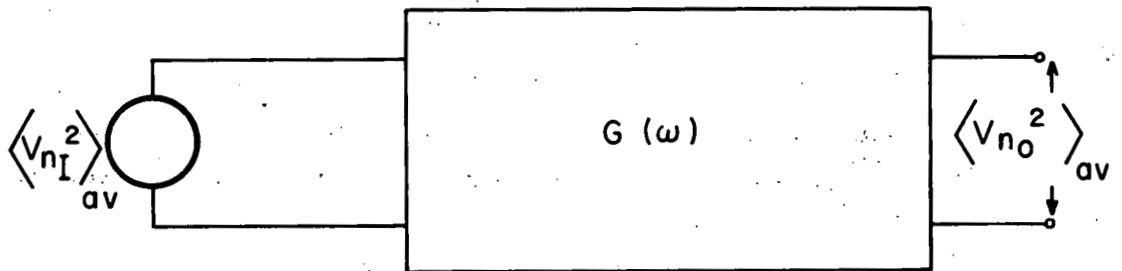
MU-25423

Fig. 9. Frequency dependence of the amplifier.

solving for t.   By combining the maximum response for a unit step $H(t_1)$ and V_{in}, the peak amplitude of the output pulse $V_{0\ peak}$ can be solved as shown in Eq. (14);

$$V_{0\ peak} = \frac{Q_{in}}{C} \cdot |H(t_1)|$$ (14)

If Eq. (14) is squared and equated to Eq. (12), then the squared effective charge that will produce an output from the amplifier equal to the mean-square noise from the amplifier can be obtained.   This charge is called Q_{eff} and is given by

$$Q_{eff} = \frac{C}{|H(t_1)|} \cdot \left(\left\langle V_{n_0}^2 \right\rangle_{av} \right)^{1/2}$$ (15)

The effective charge can be related to the effective energy by using the conversion factor of the detector (3.5 ev of energy producing about 1.6×10^{-19} coulombs of charge for the semiconductor detector):

$$E_{eff} = Q_{eff} \frac{3.5}{1.6 \times 10^{-19}} \cong 2.2 \times 10^{19} Q_{eff}.$$ (16)

The effective energy E_{eff} is the RMS fluctuation of the energy of a single energy peak.   This E_{eff} is related to the FWHM energy resolution by Eq. (17) (described previously in Sec. I):

$$E_{FWHM} = 2.35 E_{eff}.$$ (17)

VI. SUMMARY OF ANALYSIS OF RESOLUTION AND RESOLVING TIME

The equations for the effective energy corresponding to RC shaping, single-delay-line shaping, and double-delay-line shaping are solved in Appendix A, and the results are listed in Table I. The resolving-time equations for the three methods of pulse shaping are also solved in Appendix A. These results are listed in Table II. Normalized curves of the mean-square energy equations from shot noise are plotted in Fig. 10. The curves are plotted as a function of integrator and differentiator time constant in the case of RC shaping, and as a function of integrator time constant in the cases of single-and double-delay-line shaping. The single- and double-delay-line curves are plotted for four different delay-line times of 0.1 μsec, 0.2 μsec, 0.5 μsec, and 1.0 μsec. The delay-line time is twice the one-way propagation time of the shorted delay line. In Fig. 11 are curves of the effective-energy-squared equations caused by leakage and grid current, with identical parameters as Fig. 10. The curves are normalized so that the three different methods of pulse shaping can be compared for the same system. If a few parameters are known, the expected energy resolution of an alpha-particle energy-measuring system can be determined by using these curves. The parameters are:

(a) C = The detector and input capacitance of the preamplifier,

(b) g_m = The transconductance of the first tube in the preamplifier, and

(c) I_T = The bulk leakage of the detector and the grid current of the first tube.

The FWHM energy resolution is obtained as follows: one chooses the delay-line time and/or time constant at which the amplifier is to be operated. Then obtains the amount of effective squared energy from shot and current noises and adds these; then the square root is taken and multiplied by 2.35. The result will be the expected FWHM spread of the energy peak.

The resistance R from the input of the preamplifier to ground is made large enough so that its contribution to the energy spread can

Table I. Effective energy squared equations (E_{eff}^2) in ev^2.[a]

	RC shaping	Single delay-line shaping	Double-delay-line shaping
Shot noise	$4.8 \times 10^{39} \dfrac{kTC^2}{g_m \tau}$	$2.4 \times 10^{39} \dfrac{kTC^2}{g_m \tau} \dfrac{1}{1-\exp[-2\tau_0/\tau]}$	$2.4 \times 10^{39} \dfrac{kTC^2}{g_m \tau} \dfrac{3-\exp[-2\tau_0/\tau]}{1-\exp[-2\tau_0/\tau]}$
Leakage and grid current noise	$9.6 \times 10^{38} \tau q(i_G + i_L)$	$4.8 \times 10^{33} \tau q(i_G + i_L) \left\{ \dfrac{\dfrac{2\tau_0}{\tau} - (1-\exp[-2\tau_0/\tau])}{(1-\exp[-2\tau_0/\tau])^2} \right\}$	$4.8 \times 10^{38} \tau q(i_G + i_L) \left\{ \dfrac{\dfrac{4\tau_0}{\tau} - (3-\exp[-2\tau_0/\tau])(1-\exp[-2\tau_0/\tau])}{(1-\exp[-2\tau_0/\tau])^2} \right\}$
Input resistance noise	$1.92 \times 10^{39} \tau \dfrac{kT}{R}$	$9.6 \times 10^{33} \left\{ \dfrac{\dfrac{2\tau_0}{\tau} - (1-\exp[-2\tau_0/\tau])}{(1-\exp[-2\tau_0/\tau])^2} \right\}$	$9.6 \times 10^{38} \dfrac{kT}{R} \left\{ \dfrac{\dfrac{4\tau_0}{\tau} - (3-\exp[-2\tau_0/\tau])(1-\exp[-2\tau_0/\tau])}{(1-\exp[-2\tau_0/\tau])^2} \right\}$

[a] The units in this table are as follows:

$kT = 4 \times 10^{-21}$ volt-Coulombs at room temperature,

g_m in amp/volts

$q = 1.6 \times 10^{-19}$ Coulombs,

τ and τ_0 in sec, and

C in farads.

Table II. Resolving time equations (t_p) in μ sec. [a]

RC shaping	Single-delay-line shaping	Double-delay-line shaping
$\exp[\dfrac{t_p}{\tau} - 1] = \dfrac{100}{P}\ \dfrac{t_p}{\tau}$	$t_p = \tau\ \ell n\ \dfrac{100}{P} + 2\tau_0$	$t_p = 2\tau_0 + \tau\ \ell n\ \dfrac{100}{P}$ $+ \tau\ \ell n(\exp[\,2\tau_0/\tau\,] - 1)$

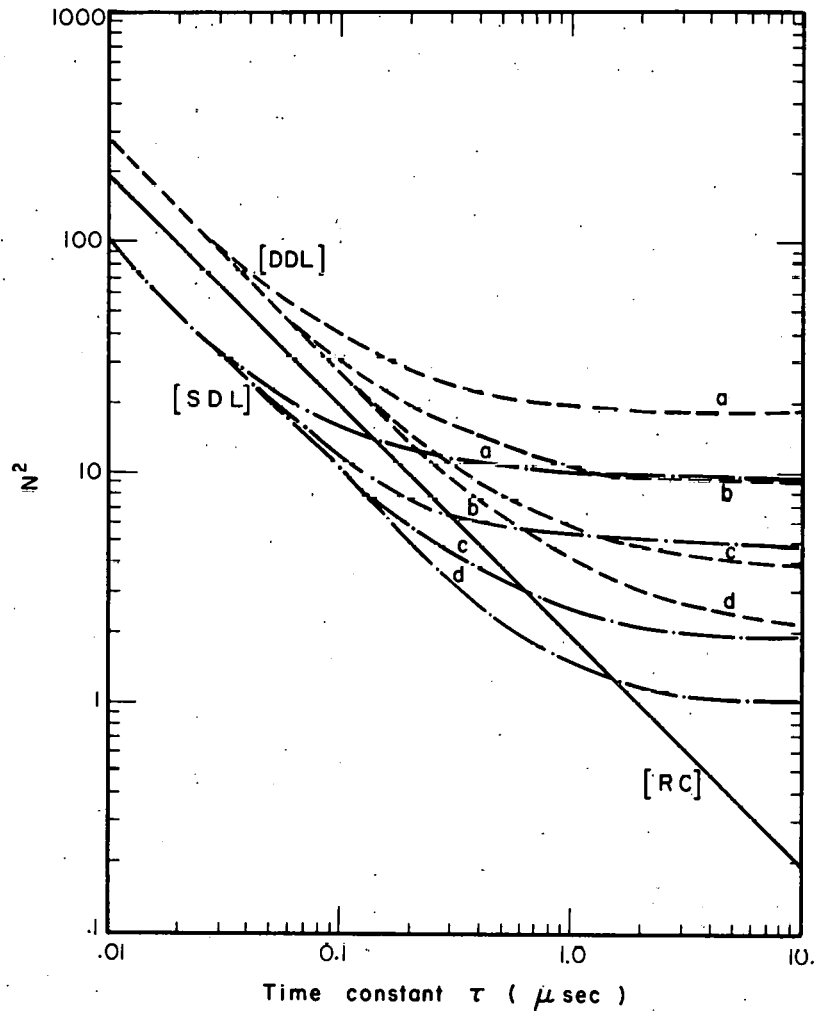[a] P is the percentage of the maximum amplitude to which the pulse has decayed in time t_p.

Fig. 10. Normalized effective-energy-squared equations from shot noise, expressed as $E_{eff}^2 = 9.7 \times 10^{24}(C^2/g_m)N^2(ev^2)$, where C is in farads, and g_m is amp/v. The shaping curves were developed from the following formulas:

$$N^2 = 2/\tau, \qquad\qquad (RC)$$

$$N^2 = \frac{1}{\tau} \ \frac{1}{1-\exp[-2\tau_0/\tau]} , \quad (SDL)$$

$$N^2 = \frac{1}{\tau} \ \frac{3-\exp[-2\tau_0/\tau]}{1-\exp[-2\tau_0/\tau]} . \quad (DDL)$$

Curves have been plotted for single- and double-delay-line times of 0.1(a), 0.2(b), 0.5(c), and 1.0(d) μsec, as indicated.

Time constant τ (μsec)

MU-25425
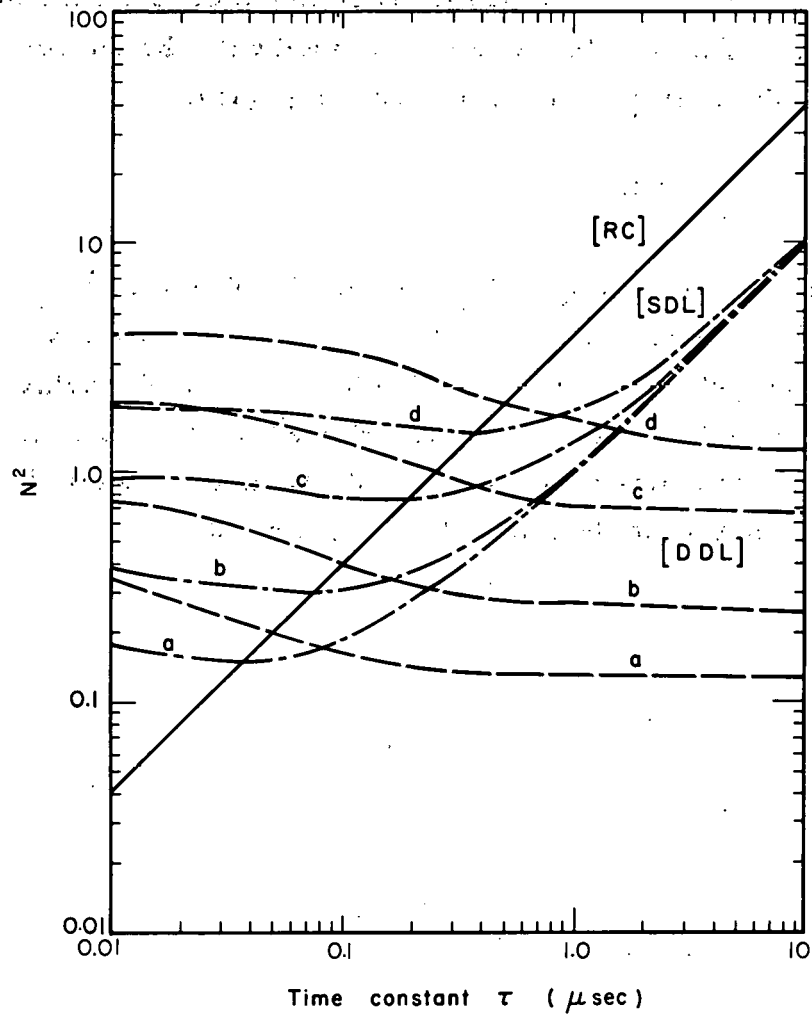
Fig. 11. Normalized effective-energy-squared equations from current noise, expressed as $E_{eff}^2 = 3.9 \times 10^{13} N^2 I$ (ev^2), where I is in amp. The shaping curves were developed from the following formulas:

$$N^2 = 4\tau, \qquad\qquad\qquad \text{(RC)}$$

$$N^2 = 2\tau \left\{ \frac{\frac{2\tau_0}{\tau} - (1 - \exp[-2\tau_0/\tau])}{(1 - \exp[-2\tau_0/\tau])^2} \right\}, \qquad \text{(SDL)}$$

$$N^2 = 2\tau \left\{ \frac{\frac{4\tau_0}{\tau} - (3 - \exp[-2\tau_0/\tau])(1 - \exp[-2\tau_0/\tau])}{(1 - \exp[-2\tau_0/\tau])^2} \right\}. \quad \text{(DDL)}$$

Curves have been plotted for single- and double-delay-line times of 0.1(a), 0.2(b), 0.5(c) and 1.0(d) μsec, as indicated.

usually be neglected. If this resistance does contribute a significant amount of noise, that can be included with the current noise by adding the additional current found from Eq. (18).

$$I_R = \frac{2kT}{qR} \tag{18}$$

where kT/q is approximately 0.025 volts at 25°C.

Figures 12, 13, and 14 are curves of the resolving time for RC shaping, single delay-line shaping, and double-delay-line shaping, respectively. The curves are plotted for the same time constants and delay-line times as Figs. 10 and 11, and are plotted for percentage error in amplitude P of 0.1%, 1%, and 10%.
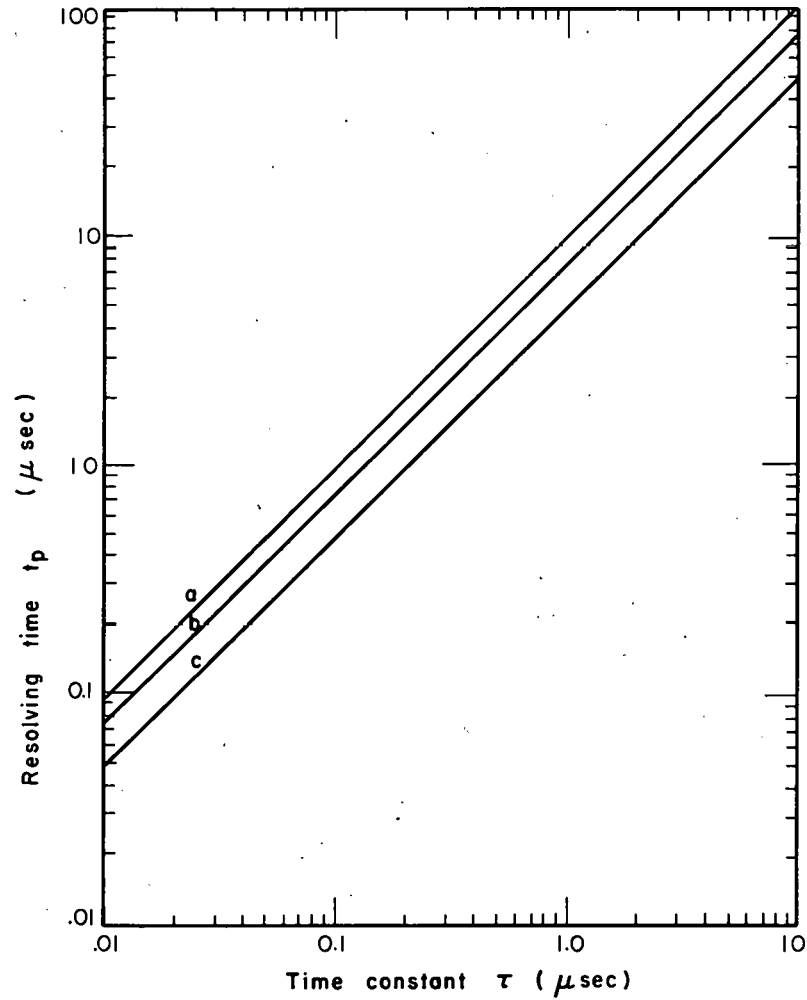
Fig. 12. Resolving time for RC shaping, plotted with amplitude errors (P) of 0.1% (a), 1.0% (b), and 10% (c). The curves were developed from

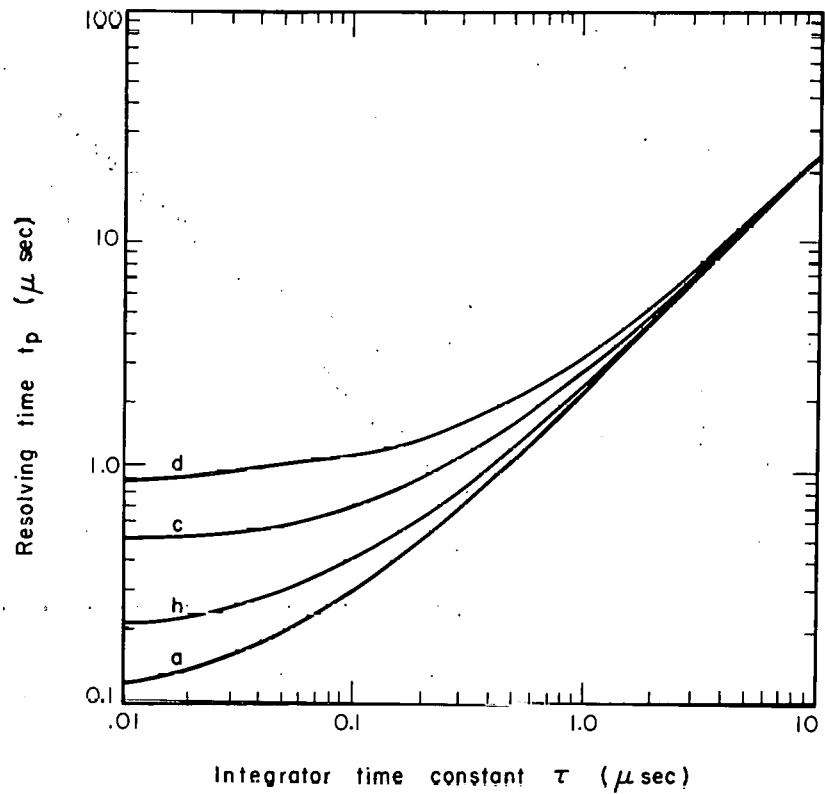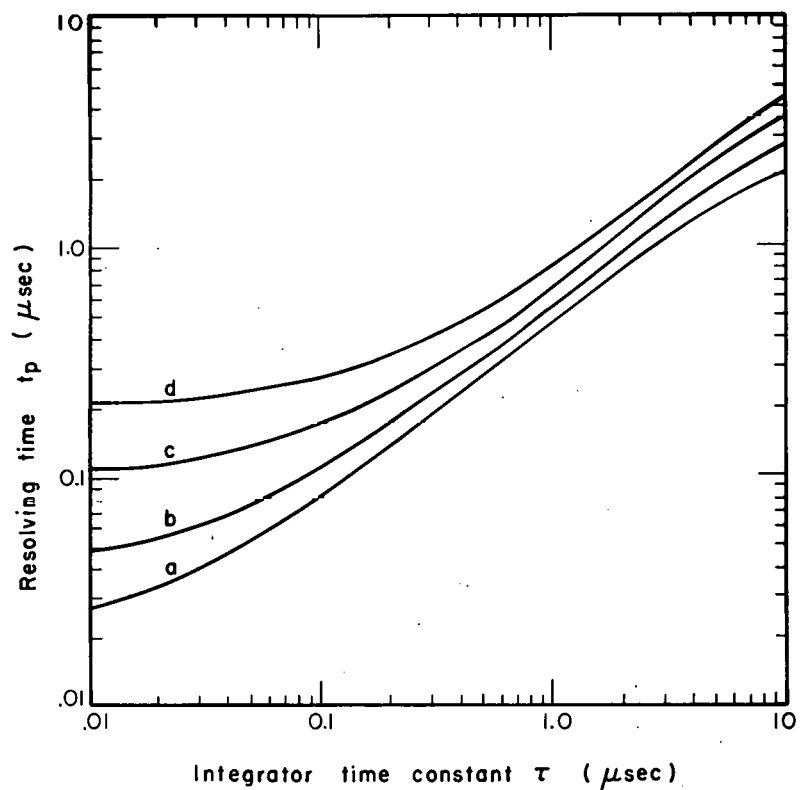$$\frac{t_p}{\tau} \cdot \frac{100}{P} = \exp\left[\frac{t_p}{\tau} - 1\right].$$
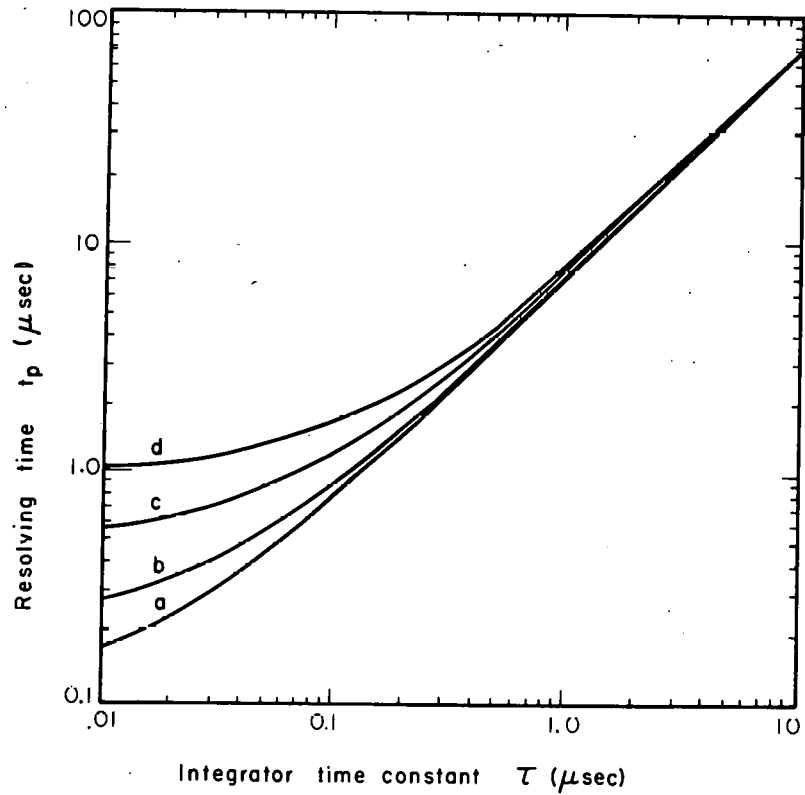
Fig. 13A. Resolving time for single-delay-line shaping.
Curves have been plotted for delay times $(2\tau_0)$ of
0.1 (a), 0.2 (b), 0.5 (c), and 1.0 (d) μsec, as indicated,
with an amplitude error (P) of 0.1%.
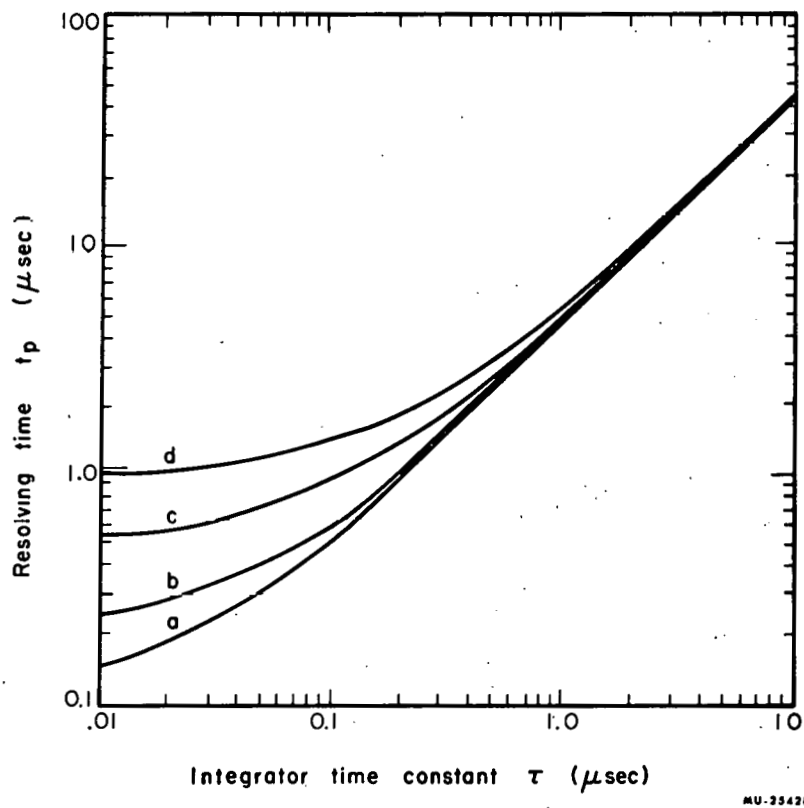
Fig. 13B. Resolving time for single-delay-line shaping.
Curves have been plotted for delay times ($2\tau_0$) of
0.1 (a), 0.2 (b), 0.5 (c), and 1.0 (d) μsec, as indicated,
with an amplitude error (P) of 1.0%.

Fig. 13C. Resolving time for single-delay-line shaping.
Curves have been plotted for delay times $(2\tau_0)$ of
0.1 (a), 0.2 (b), 0.5 (c), and 1.0 (d) μsec, as indicated,
with an amplitude error (P) of 10%.

Fig. 14A. Resolving time for double-delay-time shaping
for delay-line times ($2\tau_0$) of 0.1 (a), 0.2 (b), 0.5 (c),
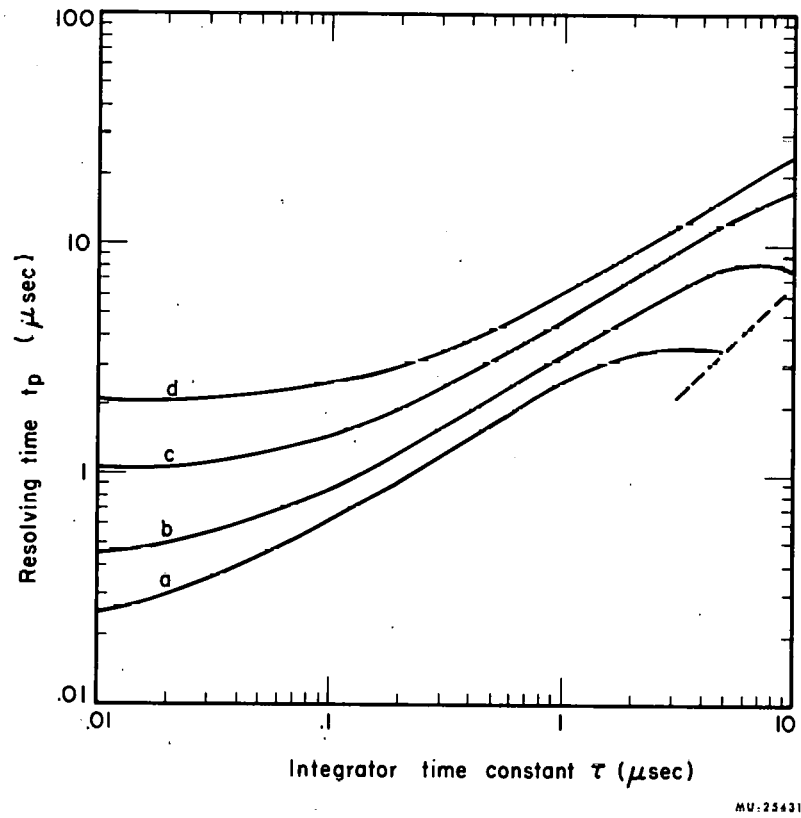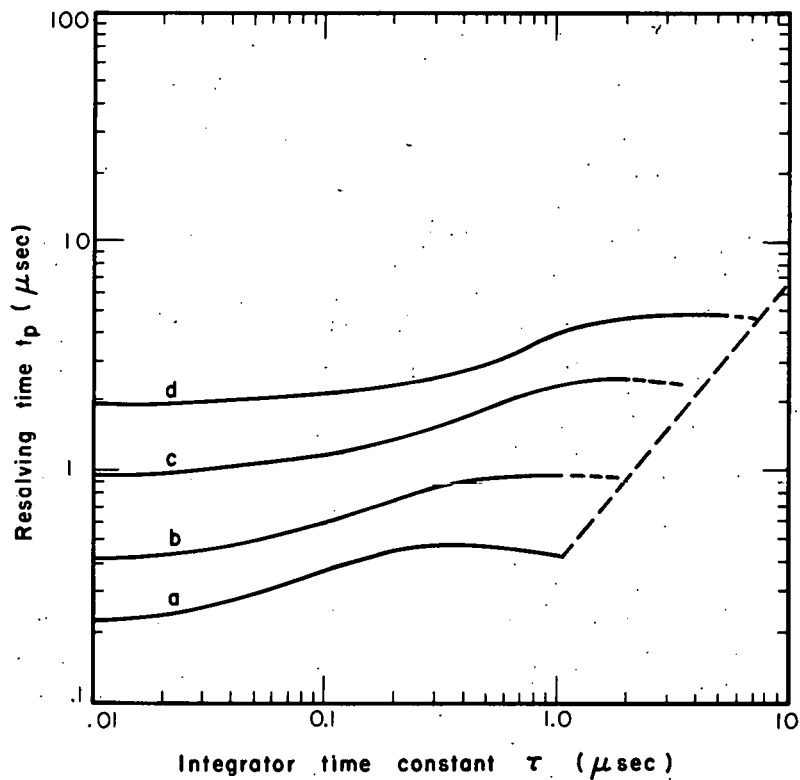and 1.0 (d) μsec, with an amplitude error (P) of 0.1%.

Fig. 14B. Resolving time for double-delay-time shaping
for delay-line times $(2\tau_0)$ of 0.1 (a), 0.2 (b), 0.5 (c),
and 1.0 (d) µsec, with an amplitude error (P) of 1.0%.
The restriction that $t_p > 4 \tau_0$ does not hold for integrator
time constants to the right of the dashed line.

Fig. 14C. Resolving time for double-delay-time shaping
for delay-line times $(2\tau_0)$ of 0.1 (a), 0.2 (b), 0.5 (c),
and 1.0 (d) μsec, with an amplitude error (P) of 10%.
The restriction that $t_p > 4\tau_0$ does not hold for integrator
time constants to the right of the dashed line.

# VII. EXPERIMENTAL VERIFICATION OF THE ENERGY RESOLUTION ANALYSIS

A. An Alternative Method for Measuring Energy Resolution

In case a pulse height analyzer is not available, the FWHM energy resolution due to noise from the amplifier system may be measured by using the equipment shown in Fig. 15.

The method of measuring the energy resolution of the amplifier system is as follows (This method assumes that the energy resolution is determined by the noise of the system and not by the defects of the detector.): (1) with the pulse generator turned off, one measures the RMS noise out of the amplifier. This measurement should be made with a power-measuring-type meter (square law) with a bandwidth at least as large as the amplifiers. A vacuum tube voltmeter such as the Hewlett-Packard 400 series can be used for this measurement, provided the bandwidth is sufficient.[11] This type of meter reads the half-cycle average of the voltage, and is calibrated to read the RMS voltage of a pure sine wave. The conversion factor from half-cycle average to RMS for a sine wave is 1.11. The noise is assumed to have a gaussian (normal) distribution, and the conversion factor from the half-cycle average to RMS of the noise voltage is 1.25; therefore the conversion factor from the RMS reading on the meter to the true RMS of the noise is 1.13. (2) The pulse generator is turned on and applied through capacitor C_a of known capacitance. The capacitor C_a should be small compared to the total capacitance of the detector and preamplifier input capacitance C, and is usually in the range of 2 to 5 pf. (3) The peak amplitude of the shaped pulse from the amplifier is measured using the oscilloscope. The FWHM energy resolution from noise is calculated from Eq. (19):

$$E_{FWHM} = \frac{V_{RMS} \; 1.13 \; C_a \; 10^{-12} \; V_{in} \; 3.5 \times 2.35}{V_{0 \; peak} \; 1.6 \times 10^{-19}} \tag{19}$$
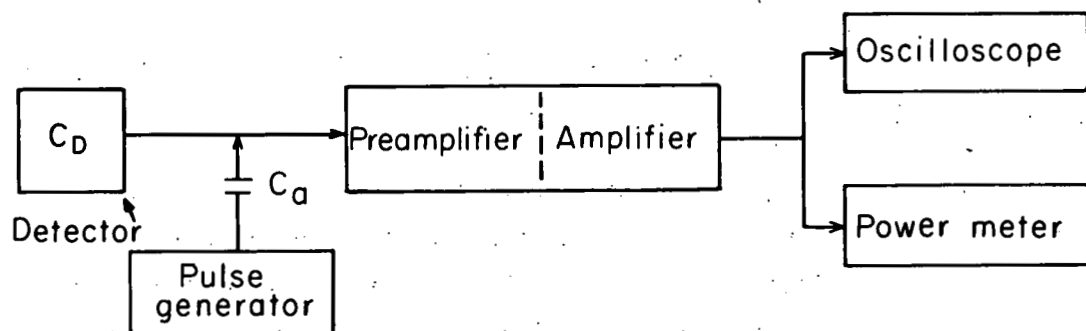
MU-25433

Fig. 15. Block diagram of equipment for measuring the
FWHM energy resolution of the amplifier system. The
pulse generator is a step or tail pulse type with a long
decay. The power meter is a square-law or average-
reading voltmeter. The capacitance $C = C_D + C_{in}$ is
the detector and input capacitance.

and

$$E_{FWHM} = 5.8 \times 10^7 \frac{V_{RMS} \, V_{in} \, C_a}{V_{0 \, peak}} \quad (ev)$$

where:

V_{RMS} = Reading on average reading VTVM calibrated for RMS of sine wave (volts),

V_{in} = Peak amplitude from step-function generator (volts),

C_a - Capacitance of series capacitor in pf,

$V_{0 \, peak}$ = Peak amplitude of pulse out of the amplifier (volts).

B. The System Used to Measure the Energy Resolution

The experimental measurements of the FWHM energy resolutions were obtained by the method described in Sec. VII-A, using a capacitor to simulate the detector capacitance. The preamplifier was an integrator type with a Western Electric WE 417-A tube in the first stage. The post-amplifier was a transistorized model with plug-in shaping circuits. A circuit of the preamplifier and a block diagram of the post-amplifier are shown respectively in Figs. 16 and 17. The parameters of the WE 417-A tube used in the preamplifier were:
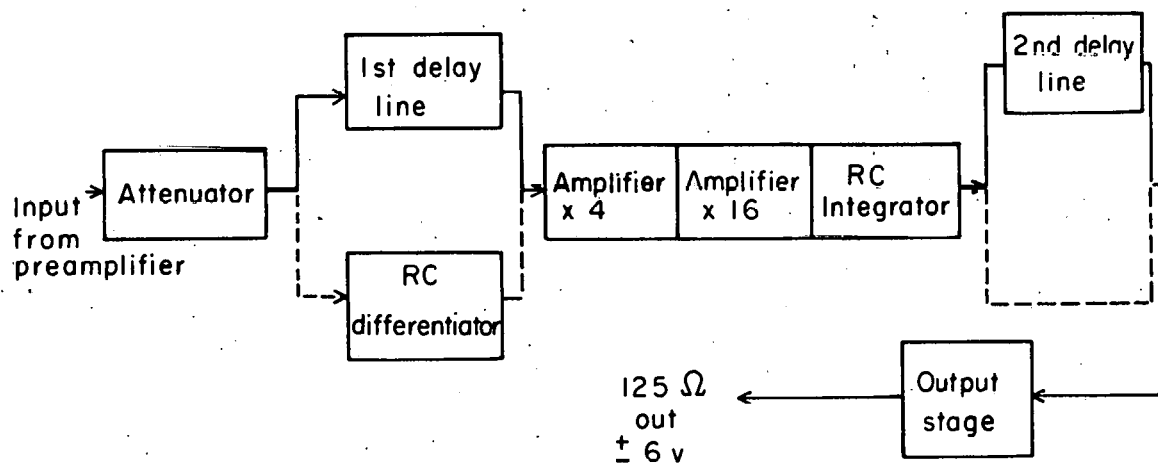
Plate voltage = 90 volts
Plate current = 10 ma
Transconductance = 16 ma/volt
Input capacitance (tube and wiring) = 22 pf

The grid current has at least two components and each component must be determined. It was assumed that an order-of-magnitude idea of the collected electronic component of grid current could be obtained by measuring the grid current with the plate voltage removed from the tube. The grid current, measured with the plate voltage applied, was assumed to be the sum of the collected and emitted electronic components. The first assumption seemed to give an order of magnitude of the electronic
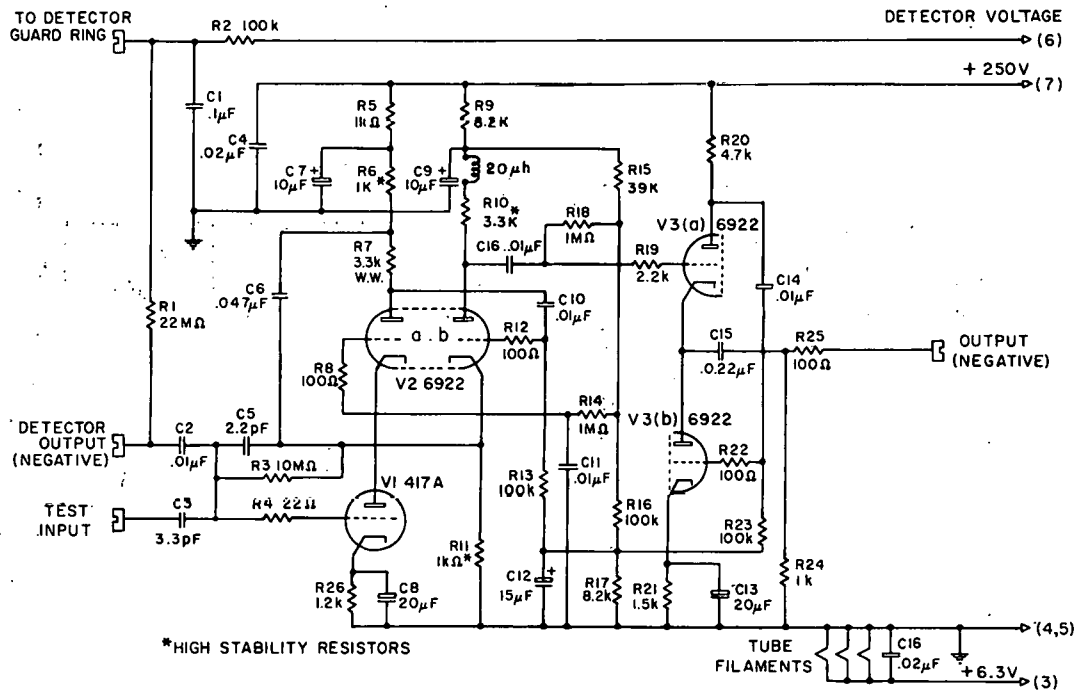
Fig. 16. Circuit of the preamplifier.

MU-21942

Fig. 17.   Block diagram of the post amplifier.

component collected by the grid, since the measured electronic com-
ponent of the current, with no plate voltage, was about four times as
high as the apparent collected electronic component of the current with
the plate voltage applied, as illustrated from the measured energy
resolution curves. The grid current was measured with the WE 417-A
tube in a test jig operating at the same plate voltage and current as the
preamplifier. The grid currents measured were:

(a) Plate voltage not applied (I_g) = -2.7×10^{-8} amp.;

(b) Plate voltage applied (I_g) = $+0.13 \times 10^{-8}$ amp.

It was assumed that there were at least two components of grid
current, and that the sum of their absolute values could be found from
the measured energy resolution curves of Fig. 18. The curve used to
determine this grid current was the lowest capacitance curve for RC
shaping at the long-time constant points, where noise is almost com-
pletely a function of grid current and source resistance. The source
resistance (detector bias and input-tube bias resistance) was 6.6 megohms.
The equivalent current caused by the resistance noise, as calculated
from Eq. (18), was 0.75×10^{-8} amp. After this equivalent current was
accounted for, the actual total grid current, as indicated by the curve,
appeared to be 1.5×10^{-8} amp. This indicated that the actual components
of the grid current in the preamplifier were:

(c) Actual component collected by grid = -0.68×10^{-8} amp;

(d) Actual component emitted by the grid = $+0.82 \times 10^{-8}$ amp.

The emitted component of grid current as calculated by Eq. (7) was
0.85×10^{-9} amp, apparently about 10 times less than the actual emitted
current, and may be explained by the fact that the grid may have emitted
electrons thermionically.

Figures 18, 19, and 20 show the measured and calculated curves
of FWHM energy resolution with respect to time constant for RC shaping,
single-delay-line shaping, and double-delay-line shaping, respectively.
The curves are plotted for three different total input capacitances of
22, 75, and 255 pf. These capacitances were used to simulate different

detector capacitances. The delay-line time is 0.25 μsec for both cases of delay-line shaping. The curves are plotted for time constants from 0.05 μsec to 5 μsec. The calculated curves used the parameters stated above, and the grid current used was $1.5 \times 10^{-8} + 0.75 \times 10^{-8}$, or 2.25×10^{-8} amp.

C. CONCLUSIONS

It is apparent from Fig. 18 that there is an optimum time constant with respect to energy resolution for amplifier systems using RC shaping. The optimum time constant for the best energy resolution depends upon the:

      (a) current (grid and leakage) and grid resistance,

      (b) transconductance of the tube, and

      (c) the input (detector, tube and wiring) capacitance.

As capacitance increases and transconductance decreases, the shot noise and the optimum time constant both increase. As the detector leakage or grid current increases and the input resistance decreases, current noise goes up and the optimum time constant gets smaller. The measured curves tend to be lower than the calculated curves at the smaller time constants; this is partly because the rise time of the preamplifier was about 0.07 μsec, and therefore the smaller time constants are not as small as indicated on the measured curves.

There is also an optimum time constant for a system using single-delay-line shaping, as shown in Fig. 19, but the optimum is much broader than in the RC case. Single-delay-line shaping may give a slight improvement in energy resolution over the RC case when the leakage or grid current is high, but because it is more complex to use, as compared with RC shaping, it probably should not be used unless the slight improvement in resolution is needed.

Figure 20 shows the curves of energy resolution for double-delay-line shaping. When the integrator time constant is short compared to the delay-line time, and when the noise is mainly shot noise, the resolution for double-delay-line shaping is about 1.4 times poorer than for single-delay-line shaping, and it fluctuates around this figure as the integrator time constant and grid current are increased. Double-delay-line shaping is usually not operated with integrator time constants that are long compared with the delay-line time, since this would cause

the resolving time to increase, and thus reduce the advantage of delay-line shaping (its ability to operate at high count rates and with overload pulses).

Figure 21 is traced from photographs of the three types of shaped pulses coming from the amplifier. The RC-shaped pulse has a 1.0-μsec integrator and differentiator time constant, the single-and double-delay-line shaped pulses have integrator time constants of 0.1 μsec and delay-line-time of 0.25 μsec.
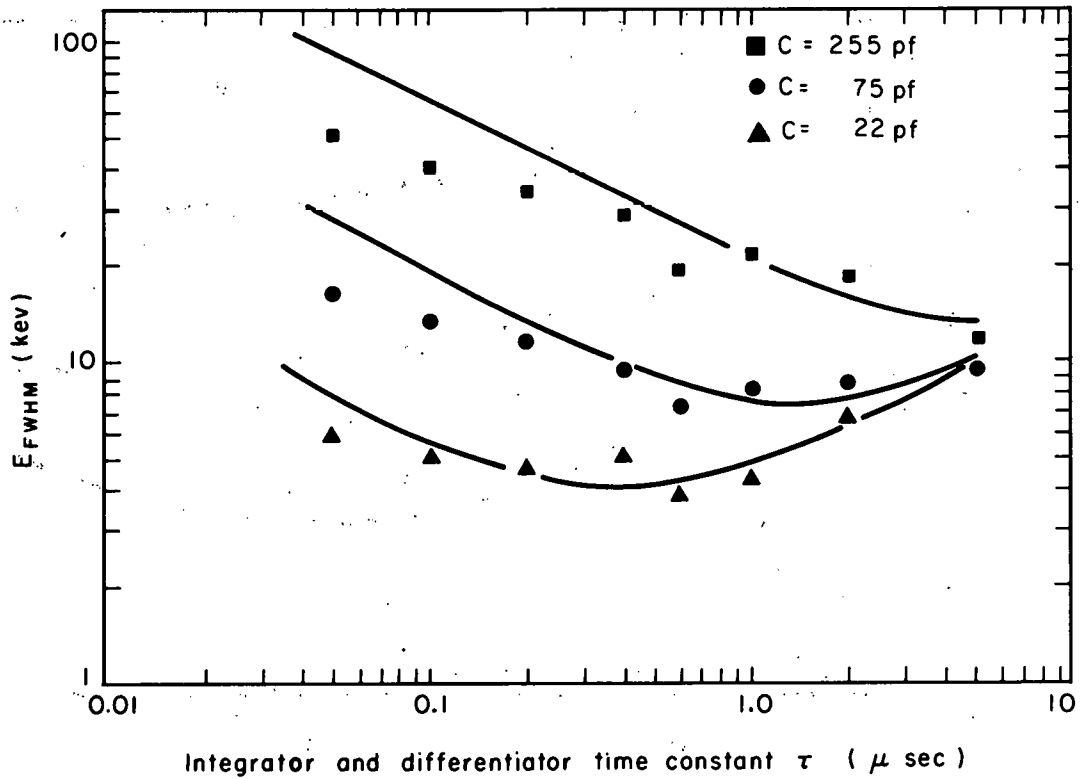
Fig. 18. Calculated and measured resolution curves for RC
shaping. Parameters are (a) I_G = 2.25×10^{-8} amp, and
(b) g_m = 16 ma/v. The curves are calculated values,
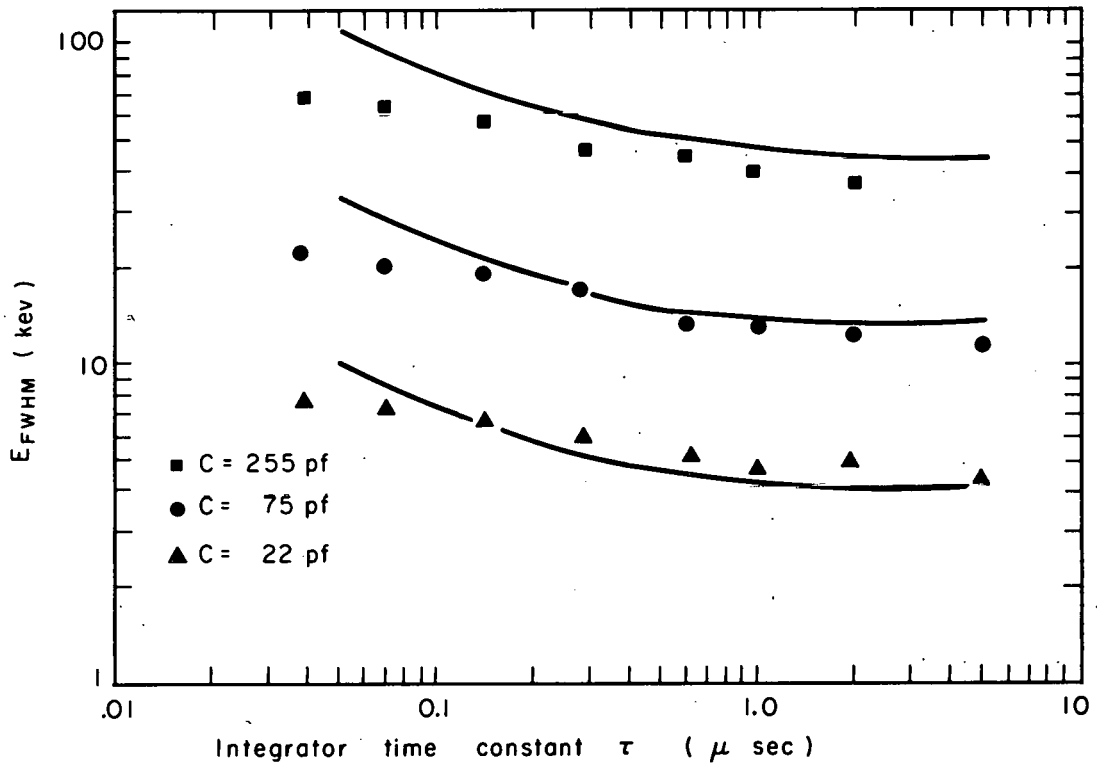and the symbols are measured values.
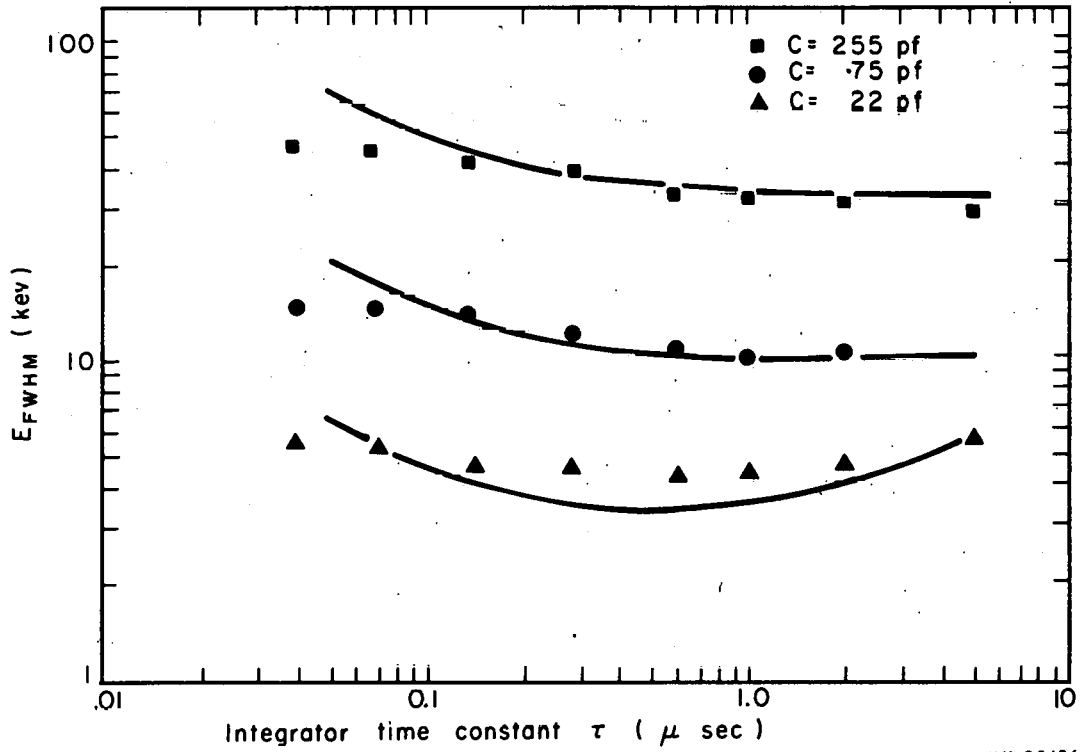
Fig. 19. Calculated and measured resolution curves for
single-delay-line shaping. Parameters are
(a) I_G = 2.25×10⁻⁸ amp, (b) g_m = 16 ma/v, and
(c) delay-line time = 0.25 μsec. The curves are
calculated values, and the symbols are measured values.

Fig. 20. Calculated and measured resolution curves for double-delay-line shaping. Parameters are (a) $I_G = 2.25 \times 10^{-8}$ amp, (b) $g_m = 16$ ma/v, and (c) delay-line time = 0.25 μsec. The curves are calculated values, and the symbols are measured values.

(a)

(b)

(c)
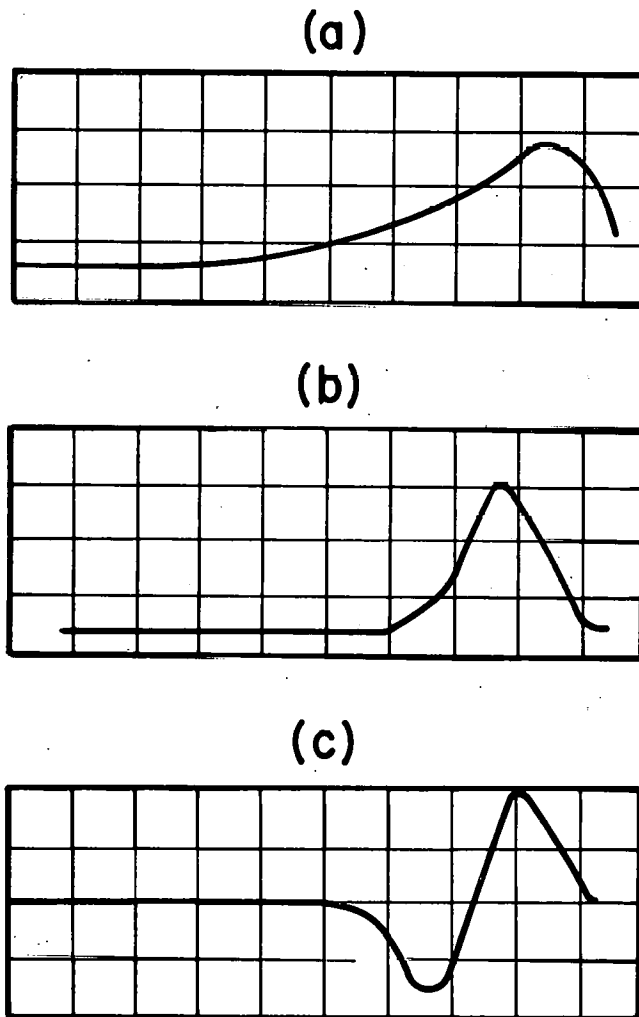
MU-25438

Fig. 21. Three drawings from photographs of shaped pulses from the amplifier: (a) RC shaped, $\tau = 1$ μsec, scope at 1 μsec/cm; (b) single-delay-line shaped, $\tau = 0.1$ μsec, 2 $\tau_0 = 0.25$ μsec, scope at 0.20 μsec/cm; and (c) double-delay-line shaped, $\tau = 0.1$ μsec, 2 $\tau_0 = 0.25$ μsec, scope at 0.20 μsec/cm.

ACKNOWLEDGMENTS

A.   Analysis of Energy Resolutions and Resolving Times

1.   Analysis of Energy Resolution for Equal Integrating and Differentiating Time-Constant (RC) Shaping

Equation (12) gives the output noise from the amplifier:

$$\left\langle V_{n_0}^2 \right\rangle_{av} = \frac{1}{2\pi} \int_0^\infty \frac{\left\langle V_{n_I}^2 \right\rangle_{av}}{df} \mid G(\omega) \mid^2 d\omega . \qquad (12)$$

The frequency dependence of the amplifier $G(\omega)$ is determined by the differentiating and integrating circuits.   Thus we have

$$\mid G(\omega) \mid = G_0 \frac{\omega\tau}{1+\omega^2\tau^2} , \qquad (20)$$

where G_0 is the voltage gain of the amplifier with the differentiating and integrating circuits removed.   The noise voltage at the amplifier input is found from Eq. (13):

$$\left\langle V_{n_I}^2 \right\rangle_{av} = \left[\frac{10\,kT}{g_m} + \frac{A}{f} + \frac{4\,kT}{R^2C^2\omega^2} + \frac{2q(I_G+I_L)}{C^2\omega^2} \right] df. \qquad (13)$$

The output-noise voltage from the amplifier, as given in Eq. (21), is obtained by using Eqs. (12), (13), and (20):

$$\left\langle V_{n_0}^2 \right\rangle_{av} = \frac{1.25\,G_0^2\,kT}{g_m\tau} + \frac{A\,G_0^2}{2} + \frac{1}{4}\,\frac{q(I_G+I_L)}{C^2}\,\tau\,G_0^2$$

$$+ \frac{1}{2}\,\frac{kT\tau}{RC^2}\,G_0^2 . \qquad (21)$$

The effective charge applied to the input of the amplifier that will produce an output equal to the root mean-square-noise voltage out of the amplifier is Q_{eff} and is given by Eq. (15):

$$Q_{eff} = \frac{C}{|H(t_1)|} \left\{ \left\langle V_{n_0}^{\,2} \right\rangle_{av} \right\}^{1/2} , \tag{15}$$

where $H(t)$ is the response of the circuit in Fig. 22 to a unit step of voltage applied to the input, and the time t_1 is the time when the response is at maximum (maximum pulse amplitude out).

$$H(t) = G_0 \frac{t}{\tau} \exp[-t/\tau] . \tag{22}$$

The time t_1 is found by taking the derivative of Eq. (22) with respect to t, and equating to zero:

$$\frac{d[H(t)]}{dt} = -G_0 \frac{t}{\tau^2} \exp[-t/\tau] + \frac{G_0}{\tau} \exp[-t/\tau] = 0 . \tag{23}$$

The solution to Eq. (23) is $t = \tau$, and the absolute value of $H(t_1)$ is given in Eq. (24):

$$|H(t_1)| = \frac{G_0}{\exp[1]} \cong \frac{G_0}{\sqrt{8}} . \tag{24}$$

The solution of Eq. (15) is:

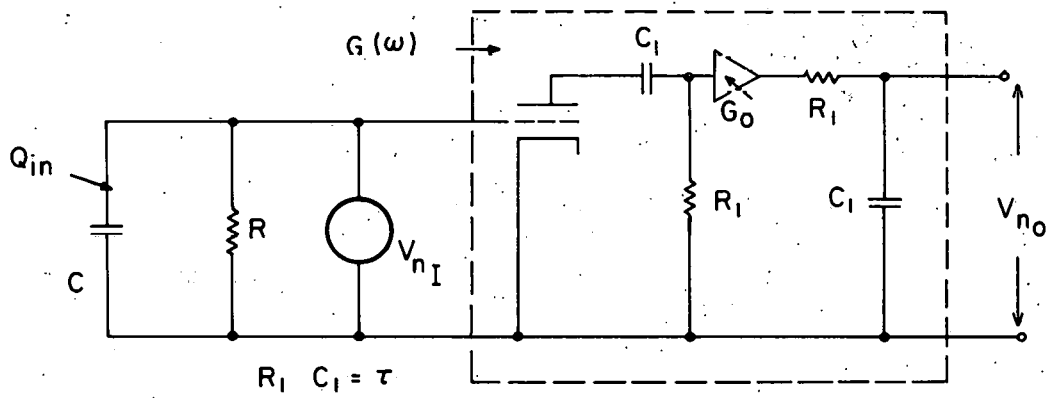$$Q_{eff}^{\,2} = \frac{10 \, kTC^2}{g_m \tau} + 4 \, AC^2 + 2\tau q (I_G + I_L) + \frac{4 \, kT \, \tau}{R} . \tag{25}$$

The effective- and full-width at half-maximum energy spread may be obtained from Eqs. (16) and (17):

$$E_{eff} = Q_{eff} \frac{3.5}{1.6 \times 10^{-19}} \cong 2.2 \times 10^{19} Q_{eff} , \tag{16}$$

and

$$E_{FWHM} = 2.35 \, E_{eff} , \tag{17}$$

Where charge is in coulombs and energy is in ev.

MU-25439

Fig. 22. Equivalent noise circuit of the amplifier for RC
shaping. C denotes the detector and tube-input capacitances,
and R is the resistance from grid to ground.

2. Resolving Time for RC Shaping for a Step Input of Voltage Applied to the Amplifier Input

The response of the amplifier to a unit step function is given by Eq. (22).

$$H(t) = G_0 \frac{t}{\tau} \exp[-t/\tau] . \tag{22}$$

A plot of this response with respect to time is shown in Fig. 23.

The time t_p is the time it takes the response to decay down to P percentage of its maximum response. Thus we have

$$H(t_p) = \frac{P}{100} \frac{G_0}{\exp[1]} = G_0 \frac{t_p}{\tau} \exp[-t_p/\tau] . \tag{26}$$

Rearranging, we obtain the resolving time equation for RC shaping:

$$\frac{100}{P} \frac{t_p}{\tau} = \exp[\frac{t_p}{\tau} - 1] . \tag{27}$$

3. Analysis of Energy Resolution for Single-Delay-Time Shaping.

The input impedance for a lossless transmission line shorted at the load end[12] is

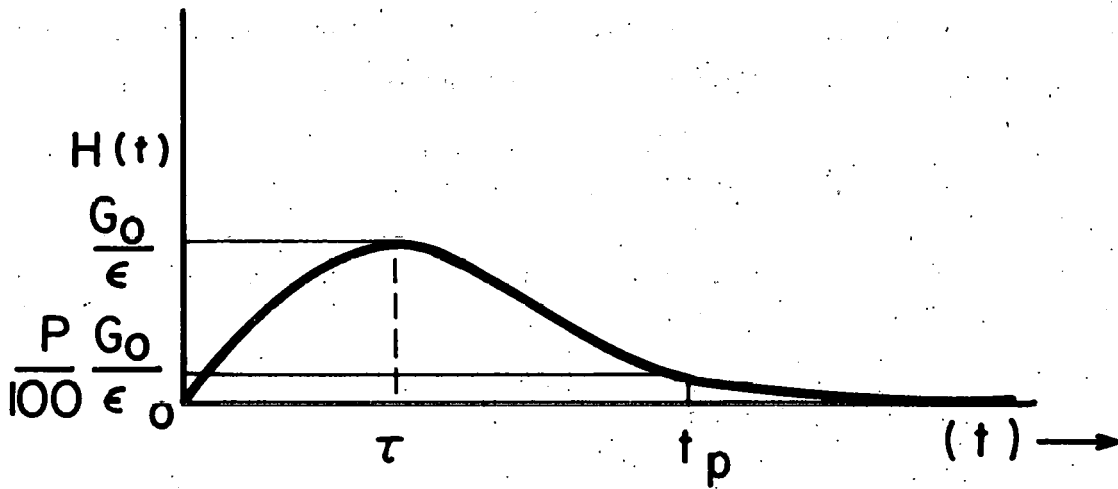$$Z_{in} = j \frac{Z_0 \sin \tau_0 \omega}{\cos \tau_0 \omega} \tag{28}$$

where Z_0 is the characteristic impedance of the transmission line and τ_0 is the one-way propagation time of the delay line.

The gain of the amplifier as a function of frequency $G(\omega)$ is given in Eq. (29).

$$G(\omega) = \frac{j G_0 \sin \tau_0 \omega}{(\cos \tau_0 \omega + j \sin \tau_0 \omega)} \frac{1}{(1 + j \omega \tau)} , \tag{29}$$

where $\tau = R_1 C_1$. The absolute value squared of $G(\omega)$ is:

$$| G(\omega) |^2 = \frac{G_0^2 \sin^2 \tau_0 \omega}{1 + \omega^2 \tau^2} . \tag{30}$$

Fig. 23.   Response of the RC shaped amplifier to a unit step
of voltage.

The output noise from the amplifier as obtained from Eq. (12), neglecting flicker noise, is given in Eq. (31) (see Appendix B for the solution of integrals used):

$$\left\langle V_{n_0}^2 \right\rangle_{av} = \frac{G_0^2 \, 1.25 \, kT}{g_m \tau}(1-\exp[-2\tau_0/\tau]) + \left[\frac{G_0^2 \, q(I_G+I_L)}{4 \, C^2}\right.$$

$$\left. + \frac{G_0^2 \, kT}{2RC^2}\right] \tau \left[\frac{2\tau_0}{\tau} - (1 - \exp[-2\tau_0/\tau])\right]. \qquad (31)$$

The response of the circuit in Fig. 24 to a unit voltage step is H(t), where

$$H(t) = \frac{G_0}{2} \left\{(1-\exp[-t/\tau]) - (1 - \exp\left[-\frac{t-2\tau_0}{\tau}\right])U(t-2\tau_0)\right\} . \qquad (32)$$
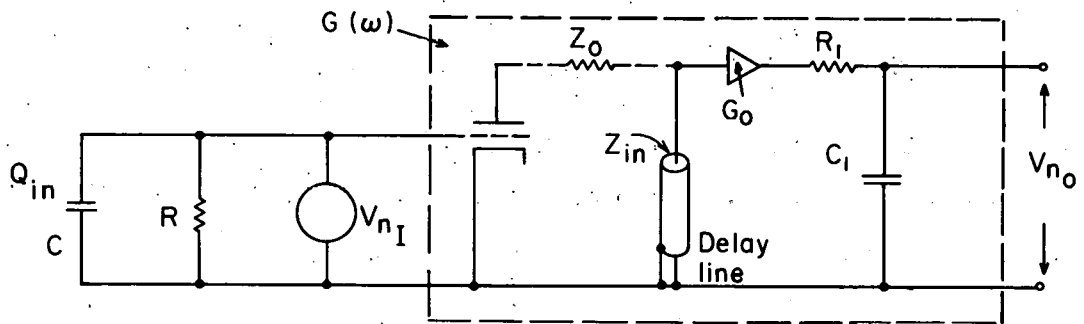
The response, as can be seen from Fig. 25, is a maximum at time $t_1 = 2\tau_0$. The absolute value of the maximum response becomes:

$$|H(t_1)| = \frac{G_0}{2} \left\{1 - \exp[-2\tau_0/\tau]\right\}, \qquad (33)$$

and the effective charge, as solved from Eq. (15), is:

$$Q_{eff}^2 = \frac{5kTC^2}{g_m \tau} \frac{1}{(1-\exp[-2\tau_0/\tau])} + \left[q(I_G+I_L) + \frac{2kT}{R}\right]$$

$$\left[\frac{2\tau_0 - \tau(1-\exp[-2\tau_0/\tau])}{(1 - \exp[-2\tau_0/\tau])^2}\right] \qquad (34)$$

The effective energy and full-width at half-maximum energy spread can be found from Eqs. (16) and (17), where Q is in coulomb and E in ev:

MU-25441

Fig. 24. The equivalent noise circuit of the amplifier for
single-delay-line shaping. C denotes the detector and
tube-input capacitances, R the grid resistance, and
$\tau = R_1 C_1$.
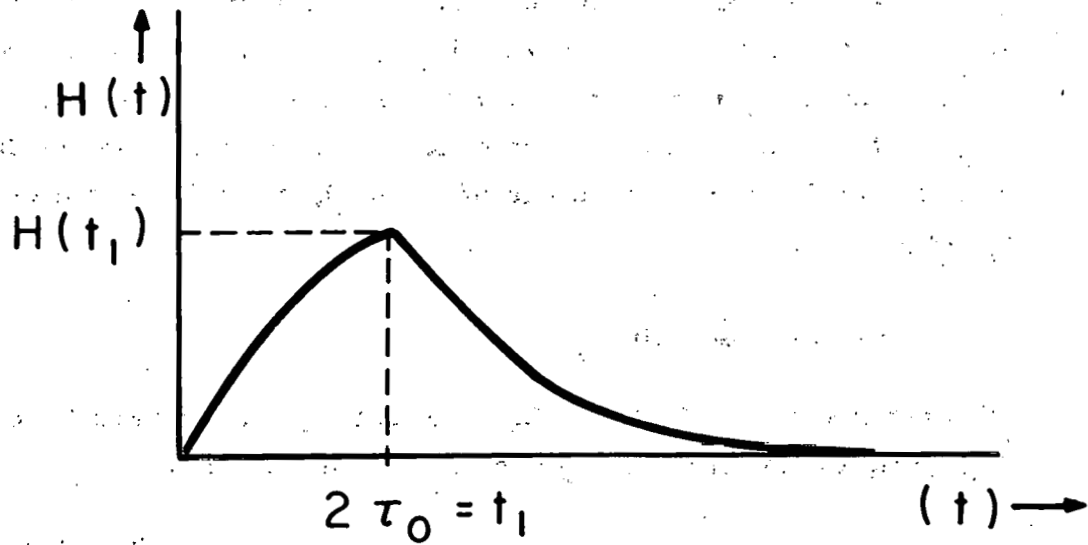
MU-25442

Fig. 25.   A typical response of the circuit in Fig. 24 to a
unit step of voltage input.

$$E_{eff} \cong 2.2 \times 10^{19} \, Q_{eff} \, , \tag{16}$$

$$E_{FWHM} = 2.35 \, E_{eff} \, . \tag{17}$$

4. Resolving Time for Single-Delay-Line Shaping for a Unit Step Input

The response of single-delay-line shaping to a unit step input is given by Eq. (32) and is shown in Fig. 26. The response is an exponential rise from $0 \leqslant t < 2 \, \tau_0$, and an exponential decay from $2\tau_0 < t \leqslant \infty$. In the figure, the time t_p is the time it takes the response to decay down to P percentage of $H(2\tau_0)$, and this response at time t_p is given by

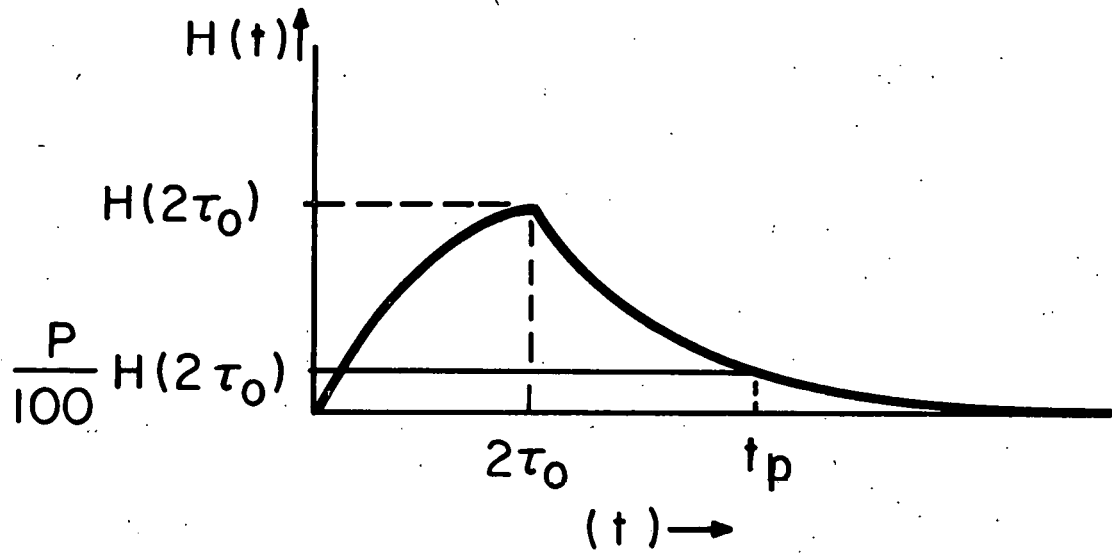$$H(t_p) = \frac{P}{100} \, H(2\tau_0) \, . \tag{35}$$

We then insert Eq. (33) into Eq. (35) and equate the results to Eq. (32), to obtain (36), the resolving time equation:

$$\frac{P}{100} (1 - \exp[-2\tau_0/\tau]) = (1 - \exp[-t_p/\tau]) - \left(1 - \exp\left[-\frac{(t_p - 2\tau_0)}{\tau}\right]\right) \tag{36}$$

$$(\text{for } t \geqslant 2\tau_0) \, .$$

When Eq. (36) is solved for t_p, Eq. (37) is obtained:

$$t_p = \tau \, \ell n \, \frac{100}{P} + 2 \, \tau_0 \, . \tag{37}$$

Fig. 26. Responses of single-delay-line shaping to a unit step of voltage input.

5. Analysis of Energy Resolution for Double-Delay-Line Shaping

The absolute value squared of $G(\omega)$ is given by Eq. (38). This equation was derived in the same manner as Eq. (30):

$$|G(\omega)|^2 = \frac{G_0^{\,2}(\sin^2 \tau_0 \omega)^2}{1 + \omega^2 \tau^2} = \frac{G_0^{\,2}(1 - \cos 2\tau_0 \omega)^2}{4(1 + \omega^2 \tau^2)} \quad . \tag{38}$$

The output noise voltage $\left\langle V_{n_0}^{\,2} \right\rangle_{av}$ (neglecting flicker noise) is found from Eqs. (12), (13) and (38):

$$\left\langle V_{n_0}^{\,2} \right\rangle_{av} = \frac{10\,kT\,G_0^{\,2}}{32\,g_m \tau} \left\{ 3 - \exp[-2\tau_0/\tau] \right\} \left\{ 1 - \exp[-2\tau_0/\tau] \right\}$$

$$+ \tau\,G_0^{\,2} \left\{ \frac{q(I_G + I_L)}{16\,C^2} + \frac{kT}{8\,RC^2} \right\} \left\{ 4\,\frac{\tau_0}{\tau} - (3 - \exp[-2\tau_0/\tau]) \right.$$

$$\left. (1 - \exp[-2\tau_0/\tau]) \right\} , \tag{39}$$

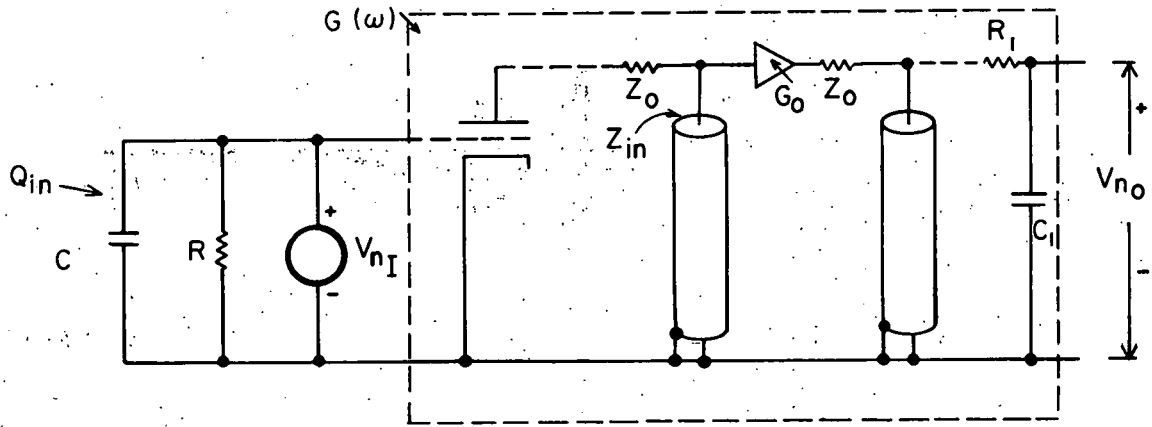in which the solution to the integrals used is in **Appendix B**.

The response of the circuit in Fig. 27 to a unit step is given by Eq. (40):

$$H(t) = \frac{G_0}{4} \left\{ (1 - \exp[-t/\tau]) - 2\left(1 - \exp\left[-\frac{t - 2\tau_0}{\tau}\right]\right) U(t - 2\tau_0) \right.$$

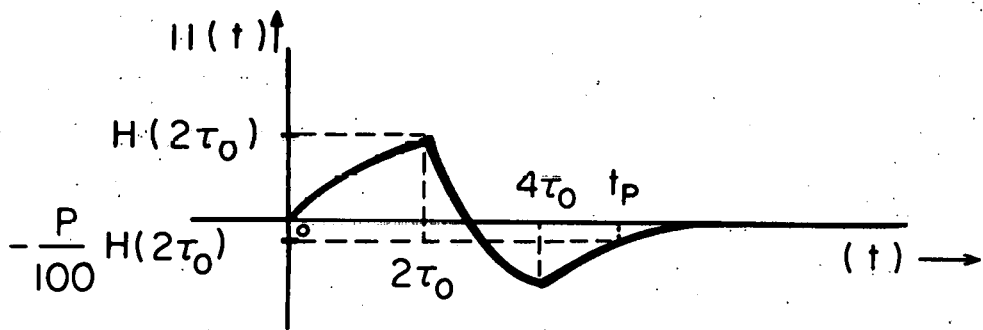$$\left. + (1 - \exp\left[-\frac{t - 4\tau_0}{\tau}\right]) U(t - 4\tau_0) \right\} . \tag{40}$$

Fig. 28 is a sketch of Eq. (40) for a typical ratio of $\frac{2\tau_0}{\tau} = 1$. The response $H(t)$ has a maximum at $t_1 = 2\tau_0$ and this maximum is given by Eq. (41).

MU-25444

Fig. 27. The equivalent noise circuit of the amplifier for
double-delay-line shaping. C denotes the detector and
tube-input capacitances, and R is the resistance from
grid to ground.

MU-25445

Fig. 28. A typical response to the circuit in Fig. 27 for a unit
step of voltage, a sketch of Eq. (40) for a typical ratio of
$2\tau_0/\tau = 1.$

$$|H(t_1)| = \frac{G_0}{4}(1 - \exp[-2\tau_0/\tau])$$ (41)

The effective charge, as solved from Eq. (15), is given by

$$Q_{eff}^2 = \frac{5kTC^2}{g_m\tau}\frac{(3-\exp[-2\tau_0/\tau])}{(1-\exp[-2\tau_0/\tau])} + \tau\left\{q(I_G+I_L) + \frac{2kT}{R}\right\}$$

$$\left\{\frac{\frac{4\tau_0}{\tau} - (3-\exp[-2\tau_0/\tau])(1-\exp[-2\tau_0/\tau])}{(1-\exp[-2\tau_0/\tau])^2}\right\} \cdot$$

(42)

The effective energy and full-width at half-maximum energy spread can be found from Eqs. (16) and (17), where Q is in coulombs and E in ev.

$$E_{eff} = 2.2\times10^{19}Q_{eff}$$ (16)

$$E_{FWHM} = 2.35\, E_{eff}$$ (17)

6. Resolving Time for Double-Delay-Line Shaping for a Unit Step Input

The response of double-delay-line shaping for a unit step input is given by Eq. (40). The time t_p is the time it takes the response to decay to P percentage of its maximum value. The resolving time equation is found from Eqs. (35), (40) and (41), for $t \geqslant 4\tau_0$. The negative sign on the left hand side of Eq. (43) indicates the decay is from the negative peak of the response (see Fig. 28).

$$-\frac{P}{100}(1-\exp[-2\tau_0/\tau]) = (1-\exp[-t_p/\tau]) - 2(1-\exp[-\frac{t_p-2\tau_0}{\tau}])$$

$$+ (1-\exp[-\frac{t_p-4\tau_0}{\tau}]).$$

(43)

Solving Eq. (43) for t_p gives us

$$t_p = 2\tau_0 + \tau \ln \frac{100}{P} + \tau \ln (\exp[2\tau_0/\tau] - 1) \tag{44}$$

B. Solution of Integrals Used in the Analysis.

These integrals were adapted from the Mathematical Tables (10th edition), and the integral tables of D. Bierens de Hann.[13,14]

(1)

$$\int_0^\infty \frac{\omega^2 \tau^2}{(1 + \omega^2 \tau^2)^2} \, d\omega = \frac{\pi}{4} \frac{1}{\tau}$$

(2)

$$\int_0^\infty \frac{\omega \tau^2}{(1 + \omega^2 \tau^2)^2} \, d\omega = \frac{1}{2}$$

(3)

$$\int_0^\infty \frac{\tau^2}{(1 + \omega^2 \tau^2)^2} \, d\omega = \frac{\pi}{4} \tau$$

(4)

$$\int_0^\infty \frac{\sin^2 \tau_0 \omega}{1 + \omega^2 \tau^2} \, d\omega = \frac{1}{\tau} \frac{\pi}{4} (1 - \exp[-2\tau_0/\tau])$$

(5)

$$\int_0^\infty \frac{\sin^2 \tau_0 \omega}{(1 + \omega^2 \tau^2) \omega^2} \, d\omega = \frac{\tau \pi}{4} \left\{ \frac{2\tau_0}{\tau} - (1 - \exp[-2\tau_0/\tau]) \right\}$$

(6)

$$\int_0^\infty \frac{(1 - \cos 2\tau_0 \omega)^2}{1 + \omega^2 \tau^2} \, d\omega = \frac{\pi}{4\tau} \left\{ (3 - \exp[-2\tau_0/\tau]) \, (1 - \exp[-2\tau_0/\tau]) \right\}$$

(7)

$$\int_0^\infty \frac{(1 - \cos 2\tau_0 \omega)^2}{(1 + \omega^2 \tau^2) \omega^2} \, d\omega = \frac{\tau \pi}{4} \left\{ 4 \frac{\tau_0}{\tau} - (3 - \exp[-2\tau_0/\tau]) \, (1 - \exp[-2\tau_0/\tau]) \right\}$$

(basic equation[14])

$$\int_0^\infty \frac{\sin^2 px}{(q^2 + x^2) x^2} \, dx = \frac{\pi}{4q^2} \left\{ 2p - \frac{1}{q} \, (1 - \exp[-2pq]) \right\}$$

REFERENCES

1. Edward Fairstein, Electrometers and Amplifiers, prepared as a contribution to the Handbook of Instruments and Techniques, Oak Ridge National Laboratory unnumbered report, February 1958 (unpublished), p. 57.

2. F. S. Goulding and W. L. Hansen, Nuclear Inst. & Methods 12, No. 2, 251 (July 1961).

3. B. G. Harvey, H. G. Jackson, T. A. Eastwood, and G. C. Hanna, Can. J. Phys. 35, 264 (1957).

4. F. S. Goulding and W. L. Hansen, Nuclear Instr. & Methods 12, No. 2, 252 (July 1961).

5. F. S. Goulding and W. L. Hansen, Nuclear Inst. & Methods 12, No. 2, 251 (July 1961).

6. Semiconductor Nuclear Particle Detectors: Proceedings of an Informal Conference, Asheville, North Carolina, September 28-30, 1960, Nuclear Science Series Report No. 32, Publication 871 (National Academy of Science - National Research Council, Washington, D. C., 1961), p. 238.

7. R. C. Chase, W. A. Higinbotham, and G. L. Miller, Amplifiers for Use with p-n Junction Radiation Detectors, IRE Trans. on Nuclear Science NS-8, No. 1, 147 (January 1961).

8. L. D. Smullin and H. A. Hans, Noise in Electron Devices (John Wiley & Sons, Inc., New York, 1959), p. 203.

9. F. S. Goulding and W. L. Hansen, Nuclear Inst. & Methods 12, No. 2, 259 (July 1961).

10. Edward Fairstein, Electrometers and Amplifiers, prepared as a contribution to the Handbook of Instruments and Techniques, Oak Ridge National Laboratory unnumbered report, February 1958 (unpublished), p. 105.

11. Edward Fairstein, Considerations in the Design of Pulse Amplifiers for Use with Solid-State Radiation Detectors, IRE Trans. on Nuclear Science NS-8, No. 1, 129 (January 1961).

12. S. Ramo and J. R. Whinney, Fields and Waves in Modern Radio
     (John Wiley & Sons, Inc., New York, 1953), p. 32.

13. Mathematical Tables from the Handbook of Chemistry and
     Physics , 10th edition (Chemical Rubber Publishing Company,
     Cleveland, Ohio, 1954).

14. Nouvelles Tables d'Intégrales Définies, edited by D. Bierens
     de Hann (G. E. Stechert and Company, New York, 1959),
     p. 252.